

1 **Supplementary information to**

2 **The synergy of morphology and mixing state on the**
3 **absorption of coated black carbon soot**

4 Johannes Heuser^{1,2,a,*}, Claudia Di Biagio^{2,*} Jérôme Yon³, Mathieu Cazaunau¹, Antonin
5 Berge^{2,b}, Edouard Pangui¹, Marco Zanatta^{1,4}, Laura Renzi⁴, Angela Marinoni⁴, Chenjie
6 Yu², Servanne Chevaillier¹, Daniel Ferry⁵, Paolo Laj^{6,c}, Michel Maillé¹, Paola Formenti²,
7 Benedicte Picquet-Varrault¹, and Jean-Francois Doussin¹

8 ¹ Univ Paris Est Creteil and Université Paris Cité, CNRS, LISA, F-94010 Créteil, France

9 ² Université Paris Cité and Univ Paris Est Creteil, CNRS, LISA, F-75013 Paris, France

10 ³ INSA Rouen Normandie, Univ. Rouen Normandie, CNRS, Normandie Univ., CORIA UMR 6614, 76000,
11 Rouen France

12 ⁴ Institute of Atmospheric Sciences and Climate, National Research Council of Italy, Bologna, Italy

13 ⁵ Aix Marseille Univ., CNRS, CINaM, Marseille, France

14 ⁶ Univ. Grenoble Alpes, IRD, CNRS, INRAE, Grenoble INP, IGE, 38000 Grenoble, France

15 ^a now at : Deutscher Wetterdienst, Frahmredder 95, D-22393 Hamburg, Germany

16 ^b now at : Laboratoire des Sciences du Climat et de l'Environnement, CEA–CNRS–UVSQ, IPSL,
17 Université Paris-Saclay, 91191 Gif-sur-Yvette, France

18 ^c now at: World Meteorological Organization, Geneva, Switzerland

19

20 *Corresponding author. Email: hannes.heu@gmail.com & claudia.dibiagio@lisa.ipsl.fr

21

22 **Contents:**

23 Supporting Text S1 to S3

24 Tables S1 to S3

25 Figures S1 to S23

26 Supplementary References

27

28 **Supporting Information Text**

29 **Text - S1. Experimental protocol of control experiments**

30 A list of all ageing experiments and control experiments considered in this study is provided in Table 1 in
31 the main manuscript. The control experiments follow the basic principle shown in Table S1. All experiments
32 start with the filling of the chamber, the injection of the soot and its characterization, which are summarized
33 in Heuser et al. (2025). Only after these steps, the ageing part of the experiments begins, which differs for
34 the individual experiments based on the objective of the study. These individual objectives and the necessary
35 protocols used are briefly discussed in the following.

36 **Soot coagulation dry:** these experiments aim to investigate the impact the time in suspensions and
37 coagulation has on the soot properties. Two experiments were performed by leaving the soot in suspension
38 for around 24 hours, i.e. the same length as for the long coating experiments. The soot was left in the chamber
39 without any other active processing, and the only injections were the constant addition of N₂ and O₂ to
40 compensate for the instrumental sampling losses. The soot properties were measured for about the first 8
41 hours and the last 4 to 6 hours using online measurements and filter samples to characterize soot from the
42 beginning to the end of the experiments. The two experiments were tested at two different soot concentrations
43 to vary the coagulation rate and get information on the impact of stronger and weaker coagulation processes.

44 **Soot coagulation humid:** these experiments targeted the investigation of the impact of relative humidity
45 and the injection protocol for water vapor on the soot properties. The humid experiments were performed
46 targeting a relative humidity of around 30% in line with the one used in coating experiments. The properties
47 of the soot in these humid conditions were measured for 5 hours with a set of filter measurements and
48 effective density scans. During this time, as also in other experiments, the water content in the chamber was
49 constantly kept stable between 25-35% by continuously compensating for the water losses due to dilution
50 during experiments.

51 **Soot irradiation dry:** the impact of irradiation on the soot aerosol was assessed in two experiments. The
52 three 6.5 kW Xenon arc lamps were used to irradiate the chamber volume, simulating solar radiation, and a
53 cryostat was used throughout irradiation time to minimize the heating effect of the lamps on the chamber
54 volume. During the whole experiment, the soot properties were measured continuously by online techniques,
55 and a set of filters, as well as effective density measurements, were taken towards the end of the 1- to 2-hour-
56 long irradiation period.

57 **Soot irradiation humid:** since the coating experiments were performed in humid conditions, the impact of
58 irradiation was also assessed in humid conditions. For this, after the initial fresh soot measurement, water
59 vapor was injected to reach an RH of around 30%. Then the compensation for the loss of water vapor due to
60 sampling was started, and the soot properties in the humid conditions were monitored using the online
61 techniques for about 80 minutes, during which an effective density scan was also made. After the scan, the
62 lamps and the cryostat were turned on, starting the irradiation of the humid soot-filled chamber. In a 3.5-
63 hour-long measurement interval, the physico-chemical properties of the soot were constantly measured, and
64 filters and density measurements were performed in the latter part of this interval while the chamber volume
65 was illuminated.

66 **Soot ozone irradiation dry and humid:** with both coating formations studied in this work relying on the
67 presence of ozone, also the impact of ozone and the presence of OH-radicals on the soot properties was
68 investigated. For this, first, water vapor was injected, following the above-discussed principle, as the first
69 step after the initial soot characterization. Then the soot in humid conditions was characterized. After about
70 60 to 90 minutes, O₃ was injected using a BMT ozone generator (BMT 802N, BMT MESSTECHNIK
71 GMBH), and the soot properties, including the effective density, were acquired in the following 80 minutes.
72 After this measurement interval, the lamps and cryostat were turned on, and the photochemical production
73 of OH-radicals and the potential photochemical ageing of soot were started. The lights were kept on for the
74 next 2 to 3 hours, and the soot properties were measured, including by multiple filter samples. This was done
75 in a total of 5 experiments.

76 **Text – S2. Coagulation estimations**

77 Calculations were performed in order to evaluate the effect of coagulation on soot processing and the likely
78 deposition of material on the soot particles.

79 In order to derive an estimate for the coagulation potential, the possible collisions of particles per unit of time
80 were calculated following (Dahneke, 1983; Fuchs et al., 1965; Otto et al., 1999; Otto and Fissan, 1999; Park
81 et al., 1999; Seinfeld and Pandis, 2016). This rate for two groups of particles i and j with the mobility size d_i
82 and d_j is defined as

$$83 \quad \frac{dN(t)}{dt} = \beta(d_i, d_j)N(d_i, t)N(d_j, t) \quad (S1)$$

84 in which $N(d_{i/j}, t)$ is the number of particles of the mobility size d_i and d_j at time t and $\beta(d_i, d_j)$ is the
85 collision kernel of these two particles. The full number of possible collisions is then calculated by integrating
86 S1 over the full range of particle sizes for d_i and d_j and adjusting to only count collisions once, resulting in:

$$87 \quad \frac{dN(t)}{dt} = \frac{1}{2} \int_{d_{min}}^{d_{max}} \int_{d_{min}}^{d_{max}} \beta(d_i, d_j)N(d_i, t)N(d_j, t) dd_i dd_j. \quad (S2)$$

88 The collision kernel $\beta(d_i, d_j)$ is calculated via:

$$89 \quad \beta(d_i, d_j) = 2\pi(d_i + d_j)(D_i + D_j)f(Kn) \quad (S3)$$

90 following (Otto et al., 1999; Otto and Fissan, 1999; Seinfeld and Pandis, 2016) and is dependent on the
91 mobility size d_i and d_j and diffusion coefficients D_i and D_j . The latter ones are determined as:

$$92 \quad D_i = \frac{kTC_c}{3\pi\mu d_i} \quad (S4)$$

93 where C_c is the slip correction factor, μ is the viscosity of air, k is the Boltzmann constant, and T is the
94 temperature. Since diffusion depends on the flow regime and the particle size distribution, spanning from the
95 diffusion to the transition regime, this is accounted for using a correction function for flow regimes, f ,
96 calculated as (Dahneke, 1983; Otto et al., 1999):

$$97 \quad f(Kn) = \frac{1 + Kn}{1 + 2Kn + 2Kn^2} \quad (S5)$$

98 The Knudsen number of the particles is related to the mean free path λ_p of the diffusing particles as:

$$99 \quad Kn = \frac{2\lambda_p}{d_{ij}} \text{ with } \lambda_p = \frac{3(D_i + D_j)}{\bar{c}_{ij}} \text{ and } \bar{c}_{ij} = \left(\left(\left(\frac{8kT}{\pi m_i} \right)^{\frac{1}{2}} \right)^2 + \left(\left(\frac{8kT}{\pi m_j} \right)^{\frac{1}{2}} \right)^2 \right)^{\frac{1}{2}} \quad (S6)$$

100 The mass m_i of each aggregate necessary for this calculation was derived using the known mass at each size
101 from the mass-resolved size measurements, used to determine the effective density.

102 Since these calculations served the aim of providing information on the soot processing, in particular after
103 the formation of nucleated secondary aerosol, calculations were adjusted to isolate the coagulation of soot-
104 containing particles as much as possible. Isolation was achieved by using the different identifiable modes of
105 the aerosol (see Fig. 1 and 2 in the main manuscript and Fig S11 to S16). The modes were used to define a
106 critical diameter $d_{min_{soot}}$, that represents the lower boundary of the size range that is dominated by soot-
107 containing particles, which in turn is used to perform a size-selective calculations.

108 These size-dependent calculations were further applied, cumulatively integrating over the measurement
109 interval t , allowing for the calculation of a cumulative coagulation that is given as relative to the initial
110 number concentration, N_0 . The final formulation is as follows:

$$111 \quad CC(t) = \begin{cases} \frac{\int_0^t \int_{d_{min_{soot}}}^{d_{max}} \int_{d_{min}}^{d_{max}} \beta(d_i, d_j) N(d_i, t) N(d_j, t) \, dd_i dd_j dt}{N_0} & \text{if } d_{min_{soot}} \geq d_{min} \\ \frac{\int_0^t \frac{1}{2} \int_{d_{min_{soot}}}^{d_{max}} \int_{d_{min}}^{d_{max}} \beta(d_i, d_j) N(d_i, t) N(d_j, t) \, dd_i dd_j dt}{N_0} & \text{if } d_{min_{soot}} < d_{min} \end{cases} \quad (S7)$$

112 The $CC(t)$ provides the relative frequency with which the particles of the original number size distribution
113 may have undergone coagulation with soot, soot-containing particles, and/or secondary aerosol particles at
114 any time t after their injection into the chamber.

115 In addition to the number of particles coagulating, a relative measure was calculated to estimate the soot mass
116 concentration potentially involved in coagulation. Since for each size, both number and effective density are
117 known, a rough estimate of how much mass may coagulate could be made following the same principle as
118 $CC(t)$. In order to compare different experiments, values were normalized using the initial mass
119 concentration, allowing estimation of the relevance of coagulation in the process of mass deposition for the
120 formation process of the coating and during the overnight ageing.

121 Results of these calculations for the six coating experiments are displayed in Fig. S9 and S10 for H_2SO_4 and
122 SOA coating, respectively. Additionally, reference data on coagulation during non-coating experiments is
123 provided. The rates from control experiments are due to the absence of a secondary species, determined
124 without a critical diameter $d_{min_{soot}}$. The best comparison is provided by the long-term ageing experiments
125 of CS1 coagulation dry 1 and 2, which differ in their initial soot concentration. The coagulation dry 1
126 experiment is comparable in initial concentration to the S_{ref} and H_2SO_4 experiments, and coagulation dry 2
127 to the SOA- S_{high} experiment.

128 The results for CS1 coagulation dry 1 and 2 show that for pure soot aerosol, the majority of potential
129 coagulation and mass coagulation is likely to occur in the first 1 to 1.5 hours after injection, beyond this the
130 possibility and thus relevance of coagulation reduces significantly. However, potential coagulation remains
131 given throughout the entire lifetime of the soot.

132 The addition of a secondary phase alters both the number size distribution and the physico-chemical
133 properties of soot. This modification affects the coagulation potential, depending on the properties of the
134 homogeneously nucleated secondary aerosol and the soot-containing particles, which are known to differ
135 between the two coating types.

136 The H_2SO_4 generation produces larger secondary particles with CMD diameters of the secondary aerosol due
137 to processing growing close to the CMD of the soot-containing particles. For these, a significant increase in
138 potential coagulation rate can be observed. Similar to the soot injection, the absolute majority of this potential
139 processing is limited to the initial 3 to 5 hours, which mainly corresponds to the measurement interval for
140 coated particles (not aged). This implies that a large number of secondary aerosol particles may coagulate
141 with the soot-containing particles. However, the relevance of this process is limited to the pre-ageing
142 measurement period in which the aerosol properties are tracked. This further implies that mass deposition
143 due to coagulation during the ageing is minimal.

144 For the α -pinene SOA, which is significantly smaller in size and strongly separated in its size distribution
145 from the soot-containing mode, the potential coagulation is significantly less. While a minimal increase in
146 coagulation rate is calculated during the first few minutes of SOA generation, this cannot be considered
147 significant. Further, it has to be noted that the potential for coagulation reduces to a minimum following the
148 SOA generation, contrasting the control and H_2SO_4 experiments in which continuous potential coagulation
149 is observed. Fig S10 shows that the potential number and especially mass coagulations are lower than in the
150 reference experiments, and the integrated potential remains rather stable after the initial SOA generation.

151 Overall, the calculations show that the coating process affects the potential for aerosol coagulation and can
152 be relevant for the processing during the simulation of atmospheric ageing. The relevance of this process,
153 however, differs depending on the secondary aerosol properties and is found to be rather negligible for SOA
154 experiments, contrasting the H_2SO_4 experiments, where the contribution has to be considered non-negligible
155 for the coating growth and simulated atmospheric ageing.

156 **Text – S3. Calculations of soot SSA from measurements and based on Mie core-shell and fixed E_{abs}**
157 **approximations**

158 The single scattering albedo of the BC-containing aerosols (SSA_{meas}) was estimated as the ratio of the
159 scattering and extinction coefficients measured during experiments, and subtracting the scattering signal by
160 the SOA and H_2SO_4 nucleating modes identified in the size distribution. To this, Mie calculations were
161 performed assuming a refractive index of 1.5-0i for the α -pinene SOA (Denjean et al., 2015; Kim et al., 2010;
162 Schnaiter et al., 2005) and 1.24-0i for H_2SO_4 (Heuser et al., 2025).

163
164 In the Mie core-shell approximation, the SSA (SSA_{MieCS}) was calculated as a function of $M_{\text{R,bulk}}$, considering
165 a selected representative soot size distribution, taken from the pre-coating phase. We assume that the volume
166 equivalent size distribution does not change, and only the particle number and coating quantity undergo
167 changes. This choice is supported based on the observation that after the coating formation, only limited
168 coagulation is ongoing, and in particular, only minimal soot-soot-coagulation (identified also in the constant
169 median diameter of the rBC measurement) occurred.

170 In the approximation of a fixed E_{abs} of 1.5 the SSA ($SSA_{\text{fixed-1.5}}$) was calculated as

171
$$SSA_{\text{fixed-1.5}} = \frac{1}{1 + 1.5 \left(\frac{1}{SSA} - 1 \right)}. \quad (\text{S8})$$

172 It should be noted that in the case of fixed E_{abs} , due to the lack of information to quantify scattering changes
173 in the two-phase system, only the impact of coating formation on absorption was considered through E_{abs} ,
174 while scattering was assumed to remain unchanged.

175
176
177

178 **Table S1.** General concept of the soot ageing experiments, with the specifics of the ageing experiments
 179 explained in Text S1.

STEP	Duration	Time in this steady condition	Action & Objective	Comment
<i>Filling the chamber with N₂ and O₂</i>	15 min	1 hour	Connecting instruments to verify the background	
<i>Soot injection + characterisation of fresh soot</i>	0.5 to 7 min	~ 2 hours	Measurement of the aerosol physico-chemical and spectral optical properties, gas phase, and chamber thermodynamic state to determine initial conditions	For soot injection, specific instruments were disconnected (TEOM, optics, gas monitors) to adjust compensation and avoid measurement instabilities by pressure changes; reconnected a few minutes later.
<i>Soot ageing including multiple steps</i>	~ 2 hours	2 to 23 hours	Measurement of the aerosol physico-chemical and spectral optical properties, gas phase, and chamber thermodynamic state to determine evolution compared to initial conditions	
<i>Instruments disconnection and pumping</i>	30 min	NA	End of experiment, chamber evacuation until the next experiment	

180

181 **Table S2.** List of full instrumentation used to determine the properties of the aerosol particulate phase during
 182 the soot experiments in CESAM, as fully described in Heuser et al. (2025). Instrument model, measured or
 183 derived parameters, time resolution, uncertainty, and main reference or specific data treatment for each
 184 technique are provided. For all optical instruments, measurements on HEPA-filter and on the aerosol-free
 185 chamber were used to determine their current instrumental background noise level, then used to determine
 186 the noise-signal-ratio. The instruments and measurements used in the present analysis are described in the
 187 main manuscript.

Instrument	Measured or derived parameter (units)	Time resolution	Associated Uncertainties		Reference
SMPS System TSI (DMA 3080 & CPC 3772; 2.0/0.2 L min ⁻¹ sheath/aerosol flow rates)	number size distribution [# cm ⁻³] in the 19.5 to 881.7 nm mobility diameter range	180 s	3% + counting error	Error propagation considering 3% DMA uncertainty in particle mobility size selection, plus counting error as the standard deviation of an assumed Poisson distribution	(DeCarlo et al., 2004)
TSI DMA 3080 + CPMA (Combustion) + CPC 3775 high	ρ_{eff} (effective density) [g cm ⁻³] from the mass-resolved number size distribution [# cm ⁻³]	30-45 min, with 180 s at each selected mass	10%	Error propagation considering DMA uncertainty, mass-to-charge uncertainty, and relative standard error of the size distribution median diameter For mass calculation, the uncertainty in the power law fit under consideration of the eff. density uncertainties is used	(Olfert and Collings, 2005) (Yon et al., 2015)
TEOM 1400a Thermo Scientific	mass concentration [$\mu\text{g m}^{-3}$]	300 s	15%	Determined from noise operating on the chamber (determined on clean chamber values and following smoothed variability)	
CPC 3775 TSI	particle number (> 4 nm) [# cm ⁻³]	1 s	10%		
SP2 Droplet Measurement Technologies (DMT)	Refractory BC (rBC) mass concentration [$\mu\text{g m}^{-3}$] rBC number size distribution [# cm ⁻³]	60 s	17%	following (Laborde et al., 2012)	(Stephens et al., 2003)
Integrating Nephelometer 3563 TSI	scattering coefficient [Mm ⁻¹] at 450, 550 and 700 nm	1 s	8%	Propagation of uncertainties from cross-calibration (against freshly calibrated Nephelometer), truncation correction, and signal-to-noise ratio (averaged for different total loss conditions)	(Anderson et al., 1996) (Massoli et al., 2009)
CAPS PM _{ex} Aerodyne	extinction coefficient [Mm ⁻¹] at 450 and 630 nm	1 s	5-6%	Propagation of uncertainties for general measurement precision (3%;(21)) and signal-to-noise ratio (averaged for different total loss conditions)	(Kebabian et al., 2007) (Massoli et al., 2010)
CAPS PM _{SSA} Aerodyne	extinction coefficient [Mm ⁻¹] 450 and 630 nm (only extinction signal used)	1 s	5-6%	Propagation of uncertainties for general measurement precision and signal-to-noise ratio (see above)	(Onasch et al., 2015)
CAPS PM _{ex} Aerodyne/ Integrating Nephelometer 3563 TSI	absorption coefficient [Mm ⁻¹] 450 and 630 nm (extinction minus scattering)	1 s	10-30%	Propagation of uncertainties from the measurements of scattering and absorption, including the uncertainties from the interpolation of the scattering signal to 630 nm	
MAAP Thermo-Scientific	absorption coefficient [Mm ⁻¹] 637 nm wavelength	60 s	12%	Provided in the instrument's literature	(Petzold et al., 2005; Petzold and Schönlinner, 2004)
MWAA (Multi-Wavelength Absorbance Analyser)	absorption coefficient [Mm ⁻¹] 375, 405, 532, 635, 850 nm	15-120 min	mean - 19%	Provided by Massabò and team (var. based on filter loading)	(Massabò et al., 2013)
PP_UniMI (Polar photometer)	absorption coefficient [Mm ⁻¹] 405, 448, 532, 635, 780 nm	15-120 min	mean - 14%	Provided by Vecchi and team (var. based on filter loading)	(Vecchi et al., 2014)
TEM JEOL® 100CXII microscope and a JEOL JEM2010	Particle imaging and morphology characterization	30 sec to 120 min		D_{pp} , D_f , and k_f as output from Bescond (Bescond et al., 2014) average used is determined using a single determination of all CS1 pictures	

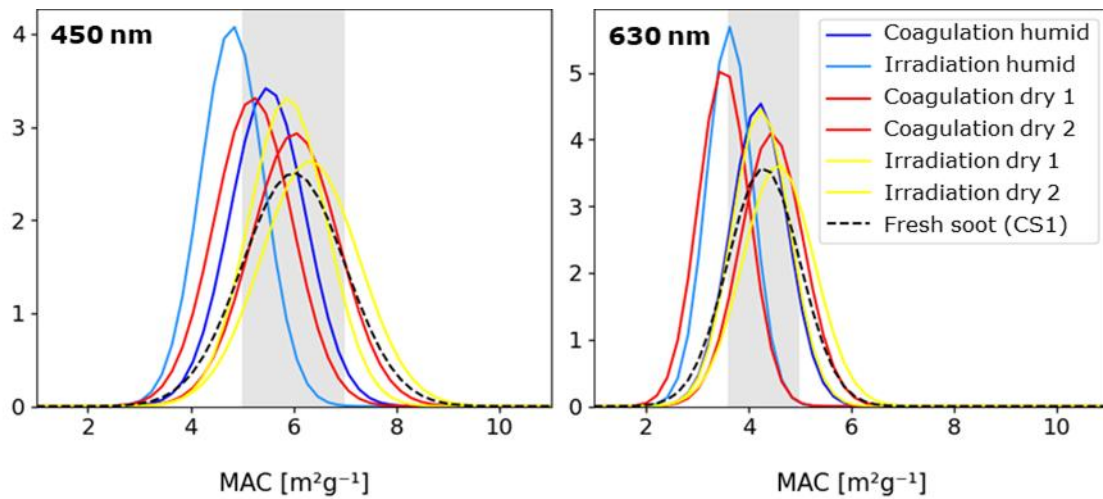
188 **Table S3.** List of instrumentation used to characterize the gas phase and the thermodynamic state of the
 189 chamber during the soot experiments in CESAM. Instrument model, measured parameters, time resolution,
 190 accuracy, and detection limit of data are provided.

Instrument	Parameter (units)	Acquisition resolution	Accuracy (at 1 min time resolution) & detection limit (Acc./DL)
NO_x Monitor – Horiba APNA370	NO, NO ₂ (NO _x) [ppb]	5 s	1 / 0.5 ppb
APEE - ProCeas	CO/CO ₂ [ppm]	45 s	0.1/ 0.05 ppm
SO₂ Monitor - Horiba APSA370	SO ₂ [ppb]	5 s	1/ 0.05 ppb
Ozone (O₃) Monitor - Horiba APOA370	O ₃ [ppb]	5 s	1 / 0.05 ppb
Teledyne T500U	NO ₂ [ppb]	30 s	0.5% (above 5 ppb)/ 0.04 ppb
Hygrometer - Vaisala HMP234	RH [%] & T [°C]	1 s	2% & ± 0.1 °C (only Acc.)
Baratron type MKS 626AX13TDE (high)/ 626AX11TDE (low)	Pressure [mBar]	1 s	0.25% for 1 to 1000 Torr (Unc.)
PTR-ToF-MS (Kore ltd.)	Mass-loading gaseous components [ppb]	60 s	0.1 ppb [DL]

191

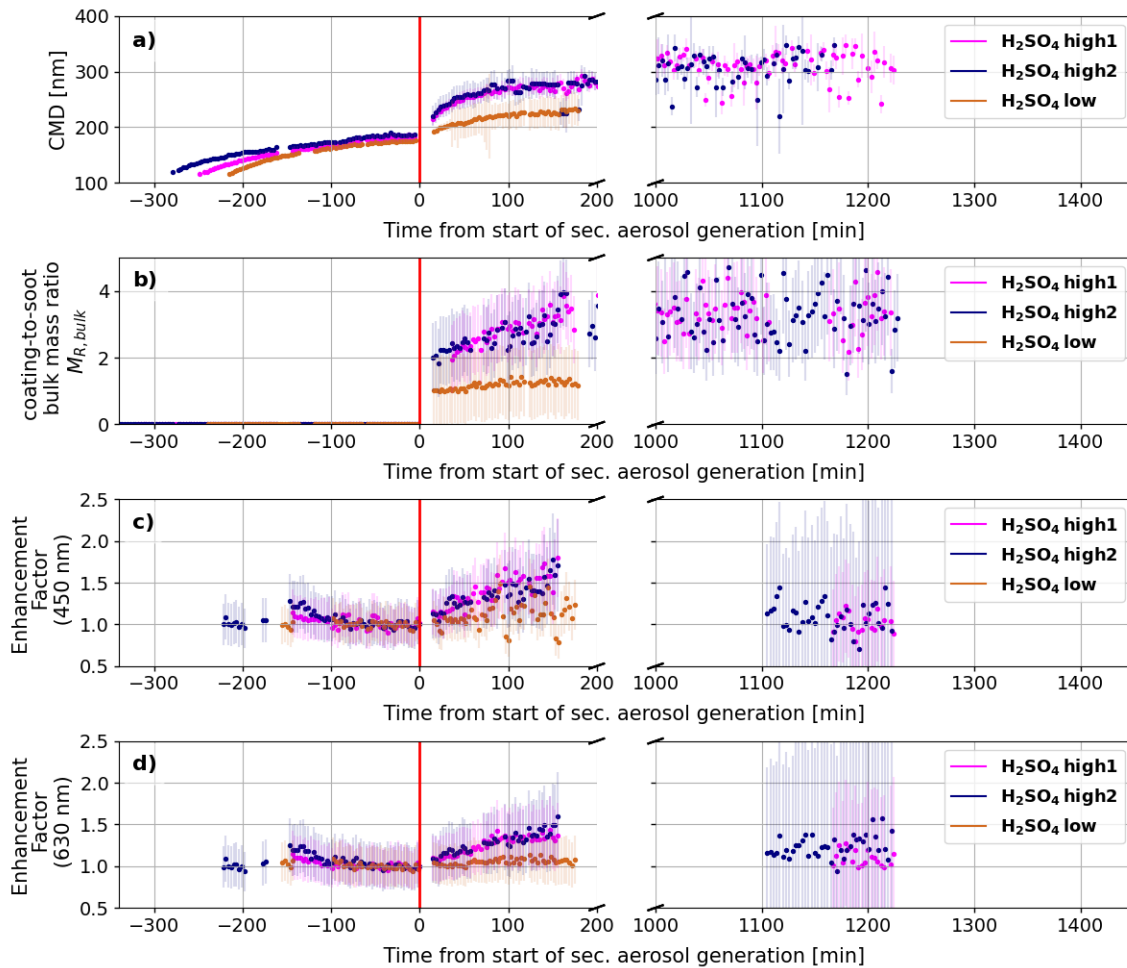
192 **Figure S1** Probability distribution of the averaged mass absorption cross sections (MAC) at 450 and 630 nm
193 for the studied control experiments. The dashed curve and the grey area represent the average and one
194 standard deviation of the probability distribution of the MAC for fresh soot measurements ($6.0 \pm 1.0 \text{ m}^2 \text{ g}^{-1}$
195 at 450 nm, and $4.3 \pm 0.7 \text{ m}^2 \text{ g}^{-1}$ at 630 nm) as reported in Heuser et al. (2025).

196



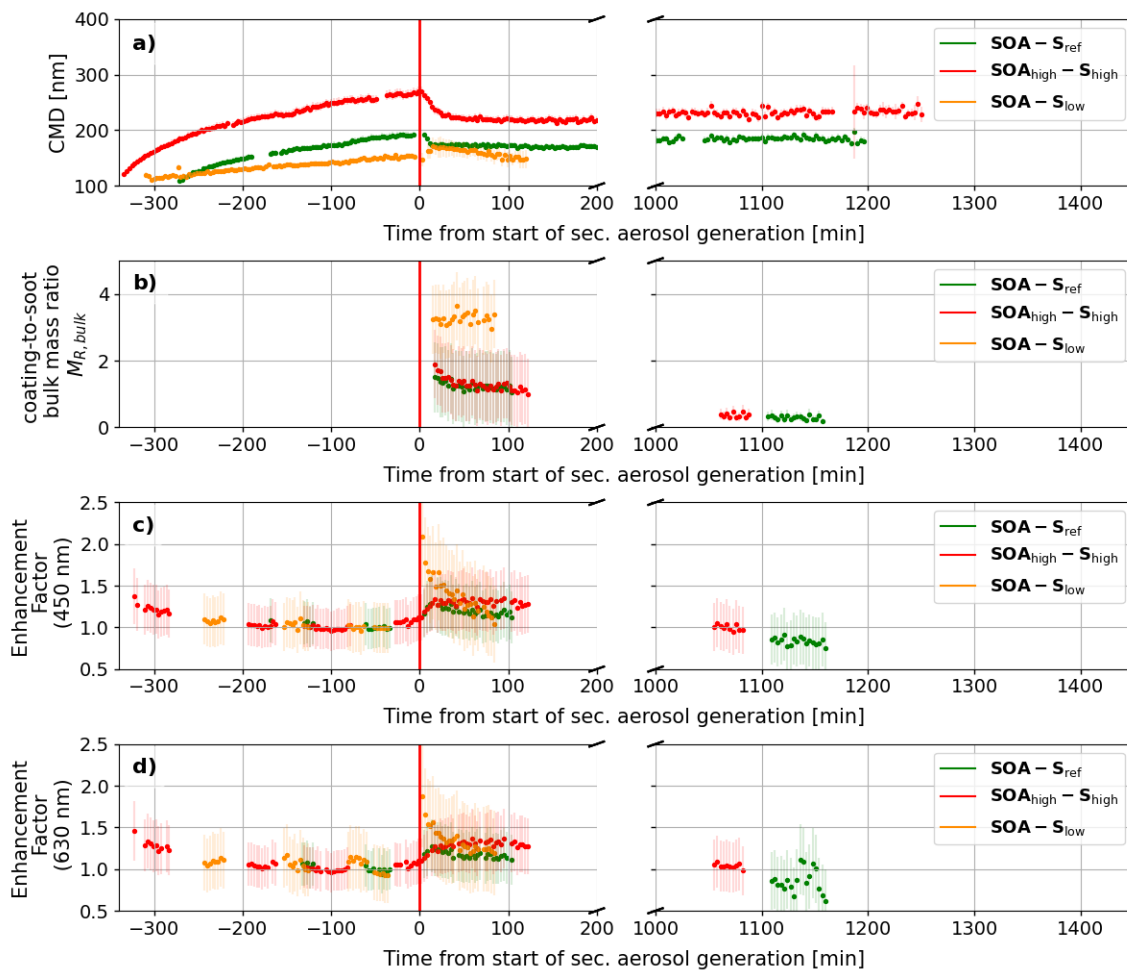
197

198 **Figure S2** Timeline for the H₂SO₄ coating experiments showing the evolution of a) the count median
 199 diameter (CMD) of the soot peak mode, b) the bulk coating-to-soot mass ratio ($M_{R,bulk}$), c) the enhancement
 200 factor of the absorption (E_{abs}) at 450 nm, and d) 630 nm.
 201



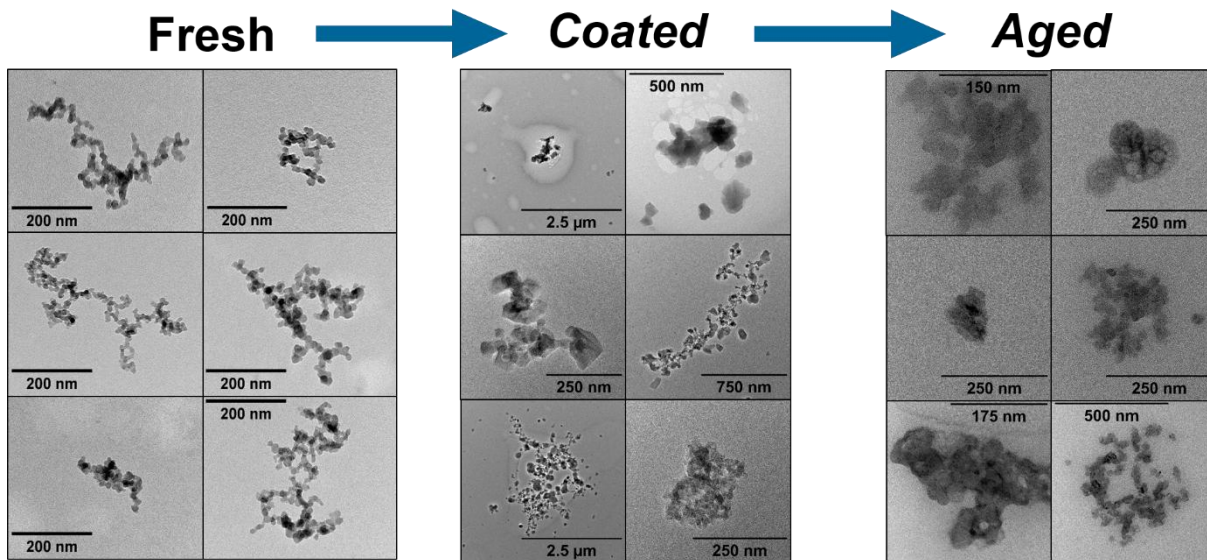
202

203 **Figure S3** Timeline for the α -pinene-SOA coating experiments showing the evolution of a) the count median
 204 diameter (CMD) of the soot peak mode, b) the bulk coating-to-soot mass ratio ($M_{R,bulk}$), c) the enhancement
 205 factor of the absorption (E_{abs}) at 450 nm, and d) 630 nm.
 206



207

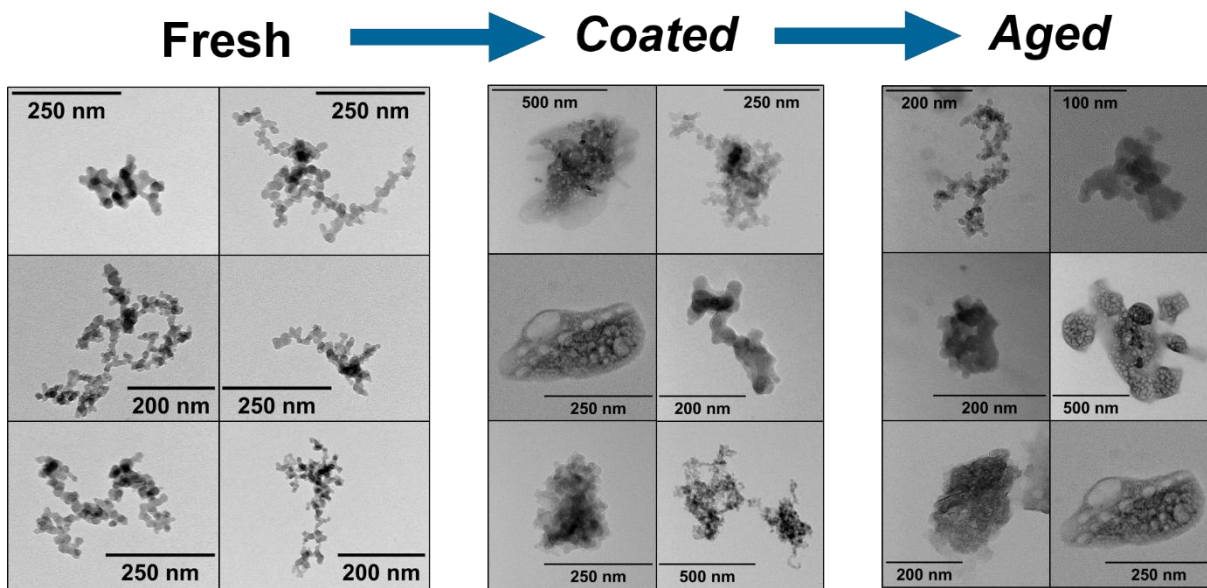
208 **Figure S4.** Overview of selected TEM images of soot containing particles from the 3 stages of the H₂SO₄
 209 coating experiments: *Fresh* (reference point for pre-coating condition; sampled about 15 to 90 min after soot
 210 injection), *Coated* (sampled about 15 to 120 minutes after start of the coating production), and *Aged*
 211 60 to 240 minutes after the long-ageing of the coated soot). Pictures are selected in order to present an overall
 212 impression of the soot structures observed.



213

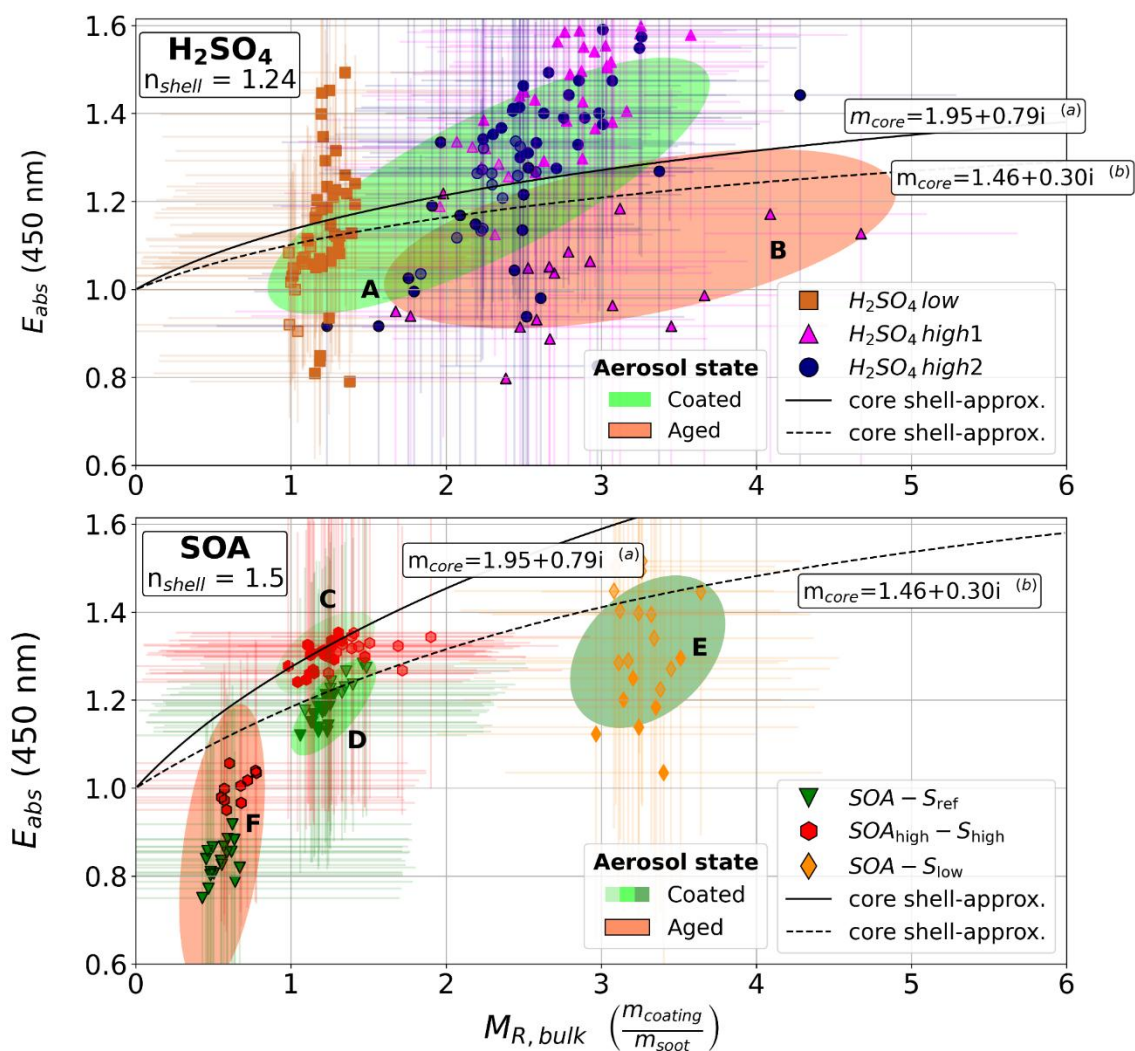
214

215 **Figure S5.** Overview of selected TEM images of soot containing particles from the 3 stages of the SOA
 216 coating experiments: *Fresh* (reference point for pre-coating condition; sampled about 15 to 90 min after soot
 217 injection), *Coated* (sampled about 15 to 120 minutes after start of the coating production), and *Aged*
 218 60 to 240 minutes after the long-ageing of the coated soot). Pictures are selected in order to present an overall
 219 impression of the soot structures observed.



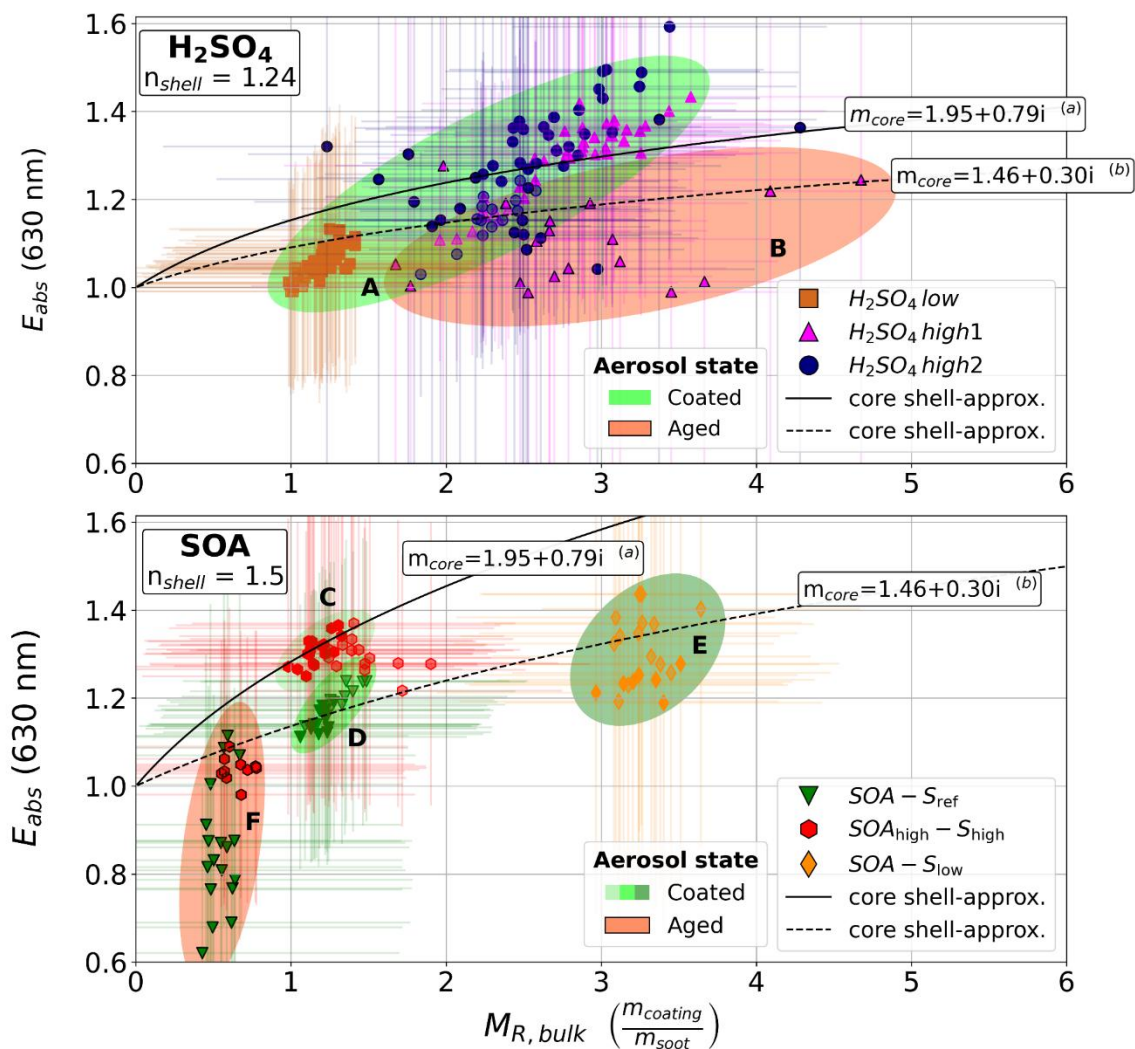
220

221 **Figure S6** Absorption enhancement factor (E_{abs}) at 450 nm as a function of the coating-soot mass ratio
 222 ($M_{R,bulk}$) for (A) the H_2SO_4 and (B) the α -pinene SOA coating experiments with their uncertainty on both
 223 variables. Symbols and color separate the measured data of different experiments. Slightly transparent values
 224 are measured during the initial 60 and points with black edges are taken after the ageing. Groupings of pre-
 225 (green) and post-ageing (red) values are manually highlighted using coloured ellipses. Additionally, the
 226 theoretical calculations using the Mie core-shell approximation for the different coating types are shown. The
 227 E_{abs} core-shell curves are reported for the value of the real part corresponding to the refractive index
 228 associated with the coating material: a value of $n_{shell}=1.5$ for the SOA and $n_{shell}=1.24$ for H_2SO_4 . The refractive
 229 index of the soot core (n_{core}) is set at a) $1.95 - 0.79i$, representative of BC based on Bond and Bergstrom
 230 (2006), and at b) $1.46-0.3i$ (Habib and Vervisch, 1988) as it represents a value on the other end of the
 231 refractive index range associated with soot.
 232



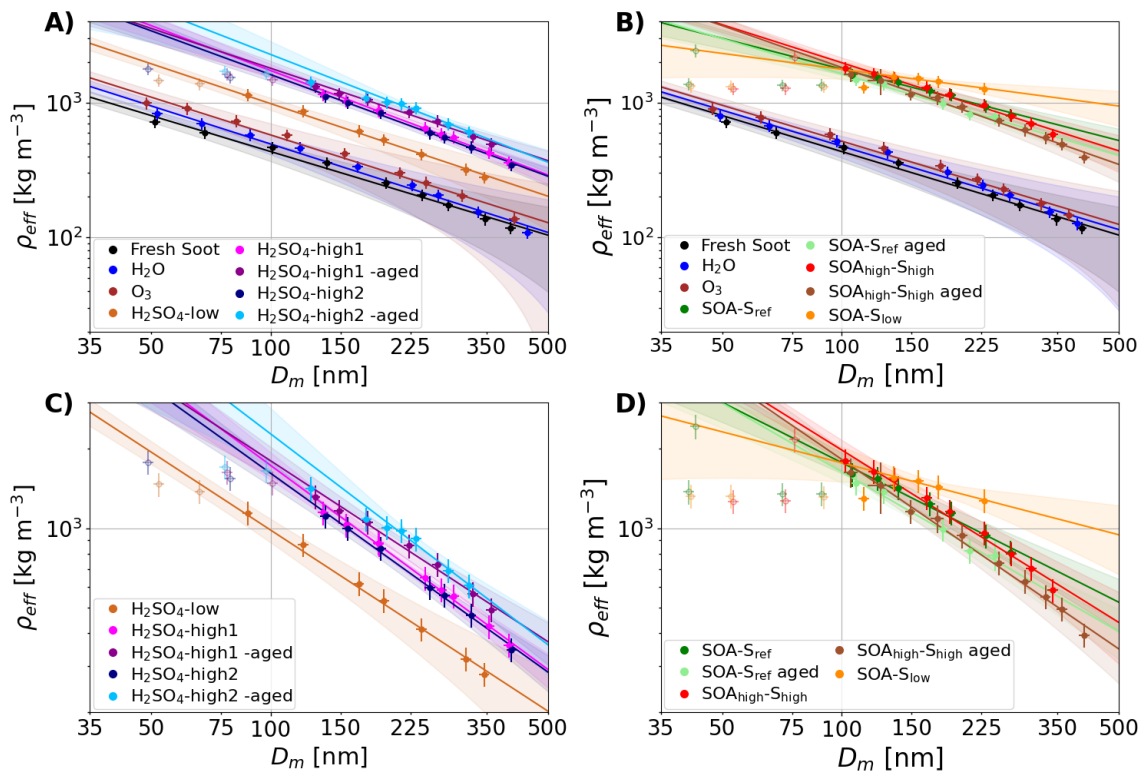
233

234 **Figure S7** Absorption enhancement factor (E_{abs}) at 630 nm as a function of the coating-soot mass ratio
 235 ($M_{R,bulk}$) for (A) the H_2SO_4 and (B) the α -pinene SOA coating experiments with their uncertainty on both
 236 variables. Symbols and color separate the measured data of different experiments. Slightly transparent values
 237 are measured during the initial 60 and points with black edges are taken after the ageing. Groupings of pre-
 238 (green) and post-ageing (red) values are manually highlighted using coloured ellipses. Additionally, the
 239 theoretical calculations using the Mie core-shell approximation for the different coating types are shown. The
 240 E_{abs} core-shell curves are reported for the value of the real part corresponding to the refractive index
 241 associated with the coating material: a value of $n_{shell}=1.5$ for the SOA and $n_{shell}=1.24$ for H_2SO_4 . The refractive
 242 index of the soot core (n_{core}) is set at a) $1.95 - 0.79i$, representative of BC based on Bond and Bergstrom
 243 (2006), and at b) $1.46-0.3i$ (Habib and Vervisch, 1988) as it represents a value on the other end of the
 244 refractive index range associated with soot.
 245



246

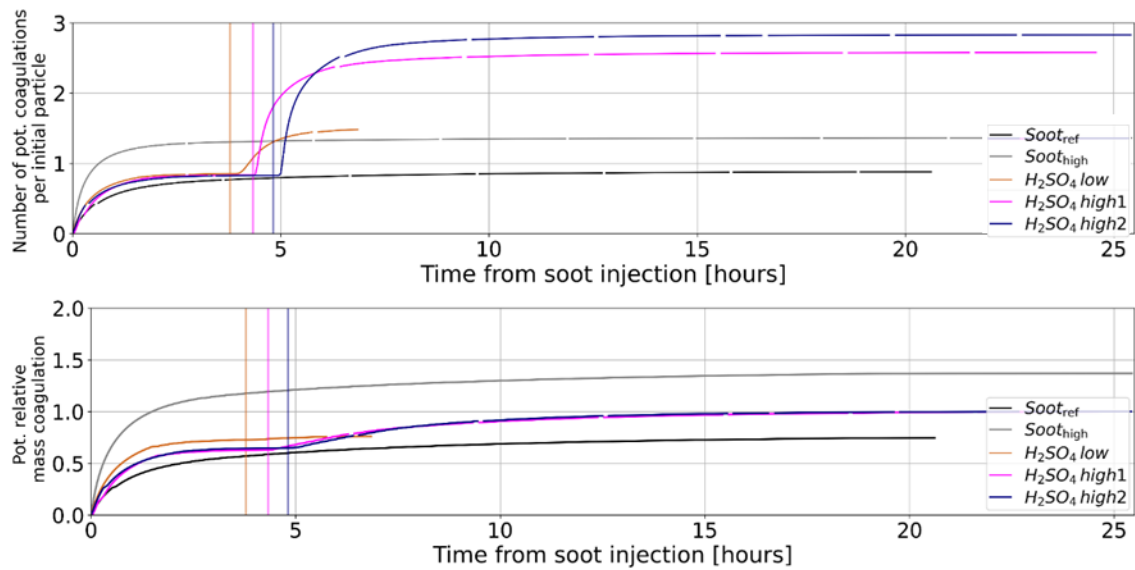
247 **Figure S8** Effective density measured as a function of the mobility diameter, $\rho_{\text{eff}}(D_m)$, for the H_2SO_4 (top)
 248 and α -pinene SOA (bottom) coating experiments. The power-law fits of $\rho_{\text{eff}}(D_m)$ based on Eq. 1 in the main
 249 manuscript (coloured lines) and the fitting uncertainties (coloured-shaded areas) are shown. As a reference,
 250 the measurements of each ageing step of H_2SO_4 -high1 (a) and SOA- S_{ref} (b) are shown with their power-law
 251 fits as both a reference for fresh soot and the time-dependent evolution of the soot properties. Error bars on
 252 single data points are omitted for clarity.



253

254 **Figure S9** Overview of the coagulation during the H_2SO_4 -coating experiments. The upper plot shows the
255 number of potential coagulation of particles with soot particles normalized with the initial particle
256 concentration as discussed in Text S2. The lower plot displays the potential mass that could coagulate onto
257 the soot, normalized by the initial mass concentration of soot particles inside the chamber. Vertical lines mark
258 the start of the secondary aerosol generation in the different experiments. Additionally, to the coating
259 experiments, these values are also given for CS1 coagulation dry 1 ($Soot_{ref}$; black) and CS1 coagulation dry
260 2 ($Soot_{high}$; grey) as a comparison for soot coagulation without secondary aerosol generation.

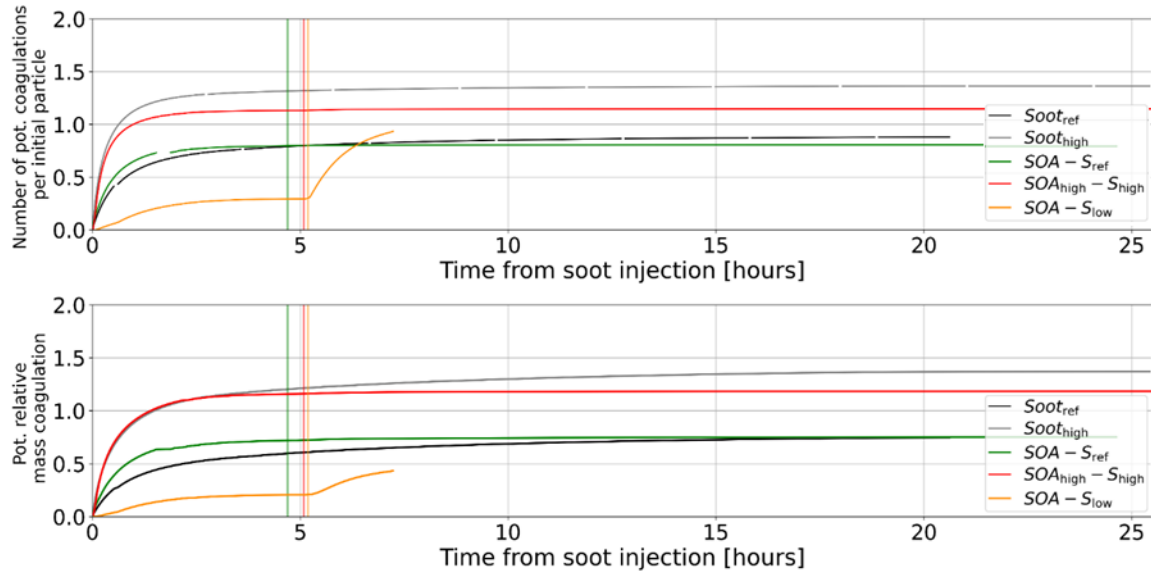
261



262

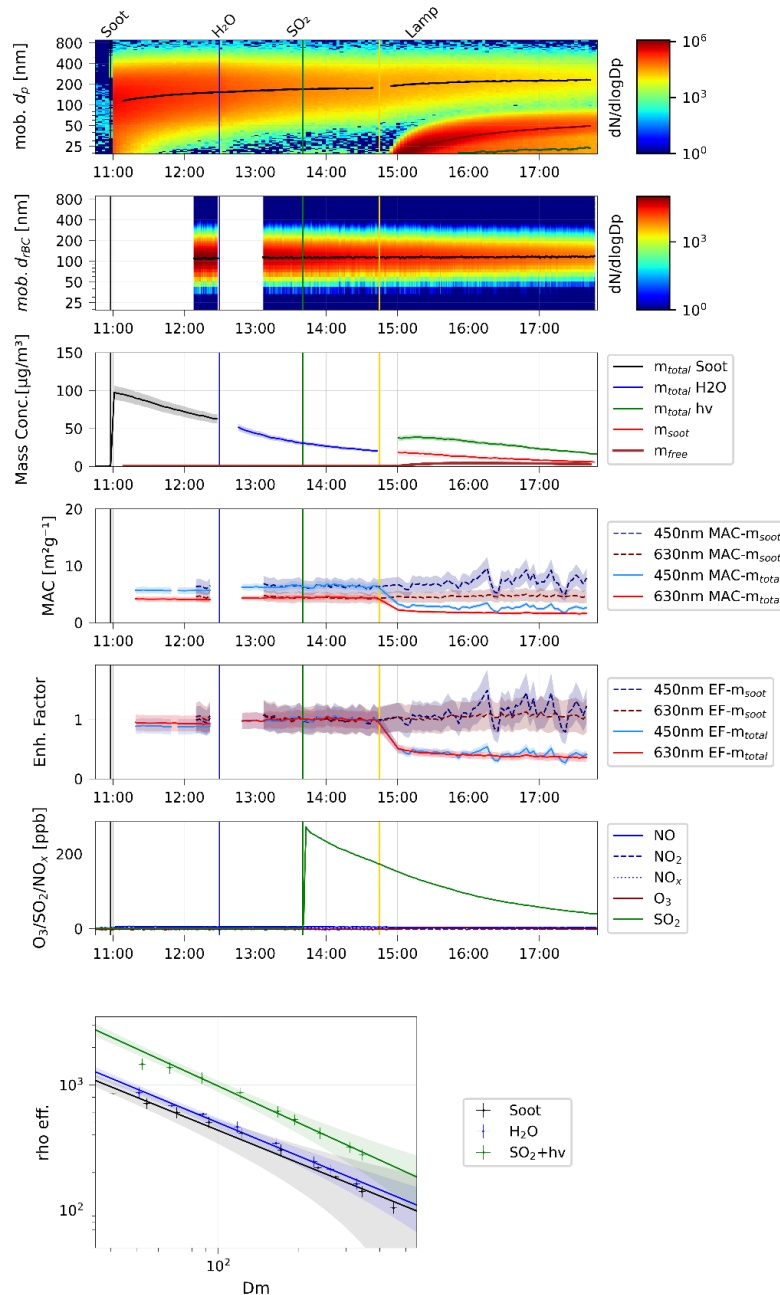
263 **Figure S10** Overview of the coagulation during the SOA-coating experiments. The upper plot shows the
 264 number of potential coagulation of particles with soot particles normalized with the initial particle
 265 concentration as discussed in Text S2. The lower plot displays the potential mass that could coagulate onto
 266 the soot, normalized by the initial mass concentration of soot particles inside the chamber. Vertical lines mark
 267 the start of the secondary aerosol generation in the different experiments. Additionally, to the coating
 268 experiments, these values are also given for CS1 coagulation dry 1 (S_{ref} ; black) and CS1 coagulation dry
 269 2 (S_{high} ; grey) as a comparison for soot coagulation without secondary aerosol generation.

270

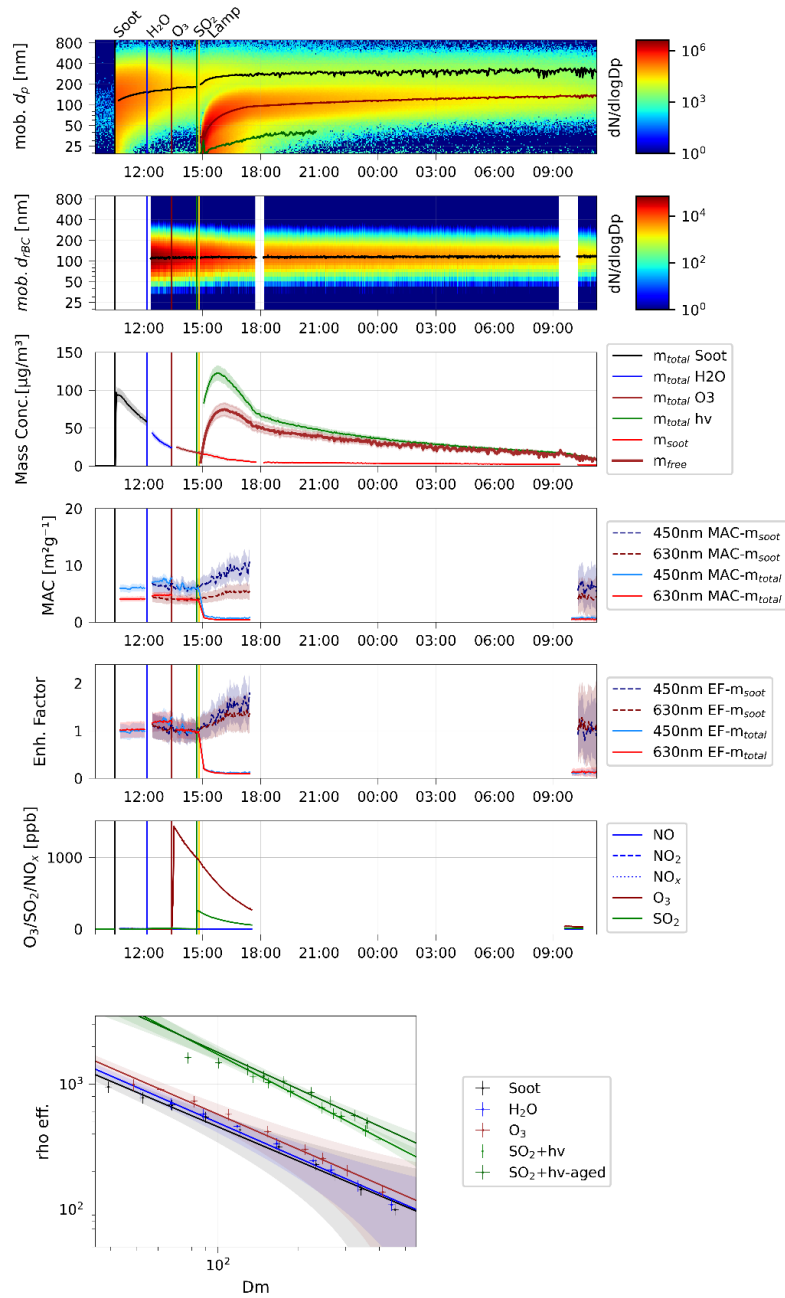


271

272 **Figure S11** Multi-panel figure of the H₂SO₄-low experiment. From top to bottom: the upper panel shows the
 273 aerosol number size distribution from the SMPS, with the fitted CMD for all modes (black=soot, other
 274 colors=secondary aerosol). Vertical lines indicate the occurrence of various events during the experiment
 275 (injection of soot, water vapor, O₃, SO₂, start and stop of irradiation (lamp and lamp off)). The second panel
 276 shows the refractory black carbon number distribution and its fitted median diameter. The third panel shows
 277 the mass concentration of the aerosol with m_{total} determined from the SMPS and different effective densities
 278 for each event (different colors), the mass of the nucleated secondary aerosol (m_{free}, indicated as m_{nuc} in the
 279 main manuscript), and the m_{soot} from the SP2. Panel four displays the mass absorption cross section (MAC)
 280 at 450 and 630 nm calculated with both m_{soot} and m_{total}. The absorption enhancement factor (E_{abs}) is shown
 281 in the fifth panel. Panel six shows the gas concentration of a selection of gases. The bottom panel shows the
 282 effective density measurements done during this experiment.

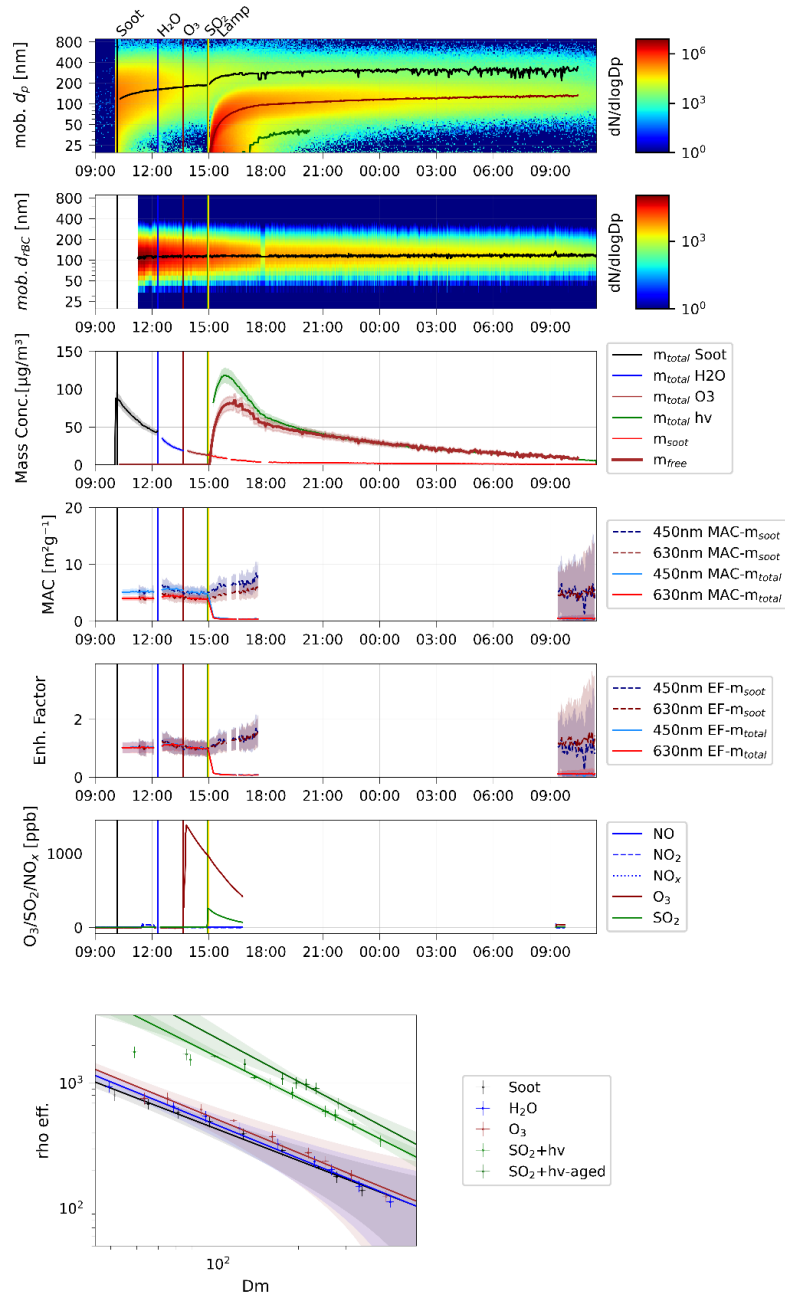


284 **Figure S12** Same as Fig. S11 for the H₂SO₄-high1 experiment.
 285



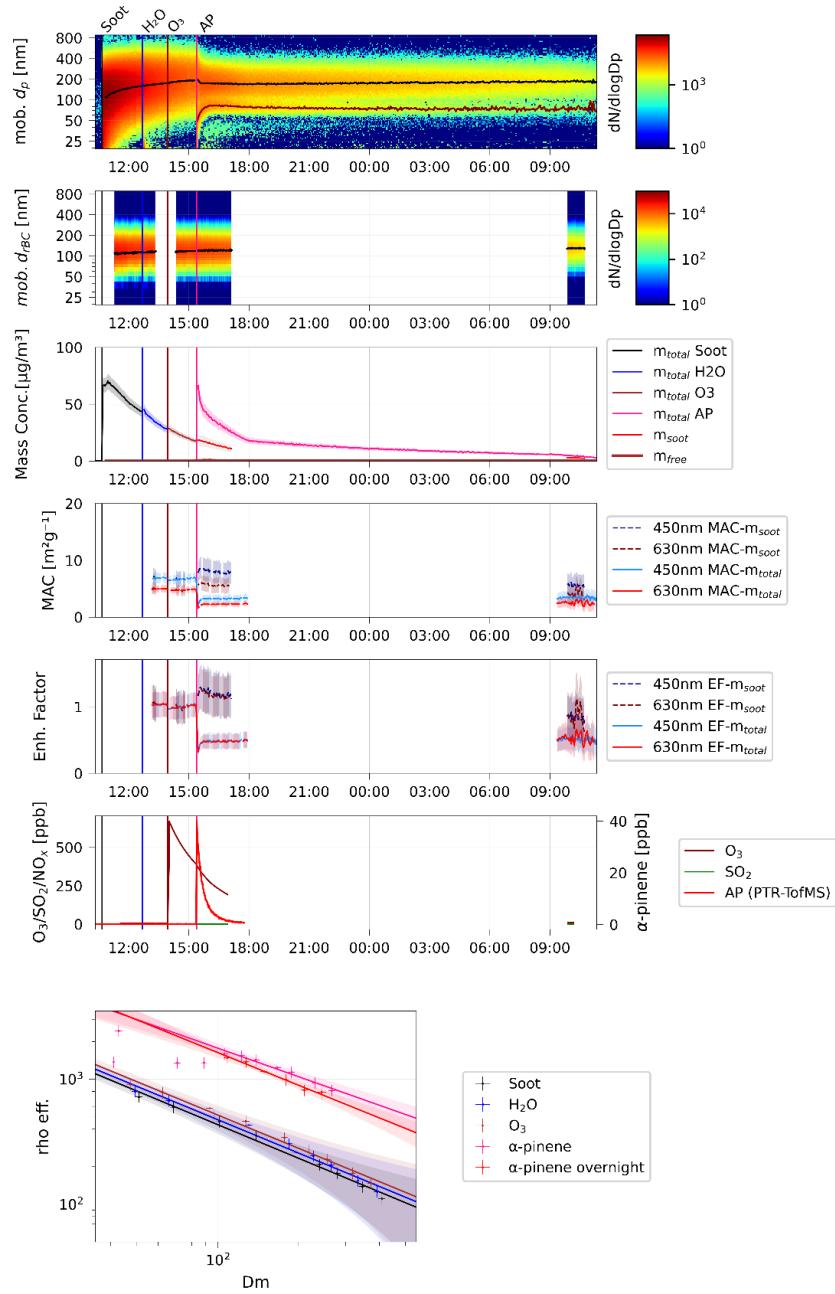
286

287 **Figure S13** Same as Fig. S11 for the H2SO4-high2 experiment.
 288



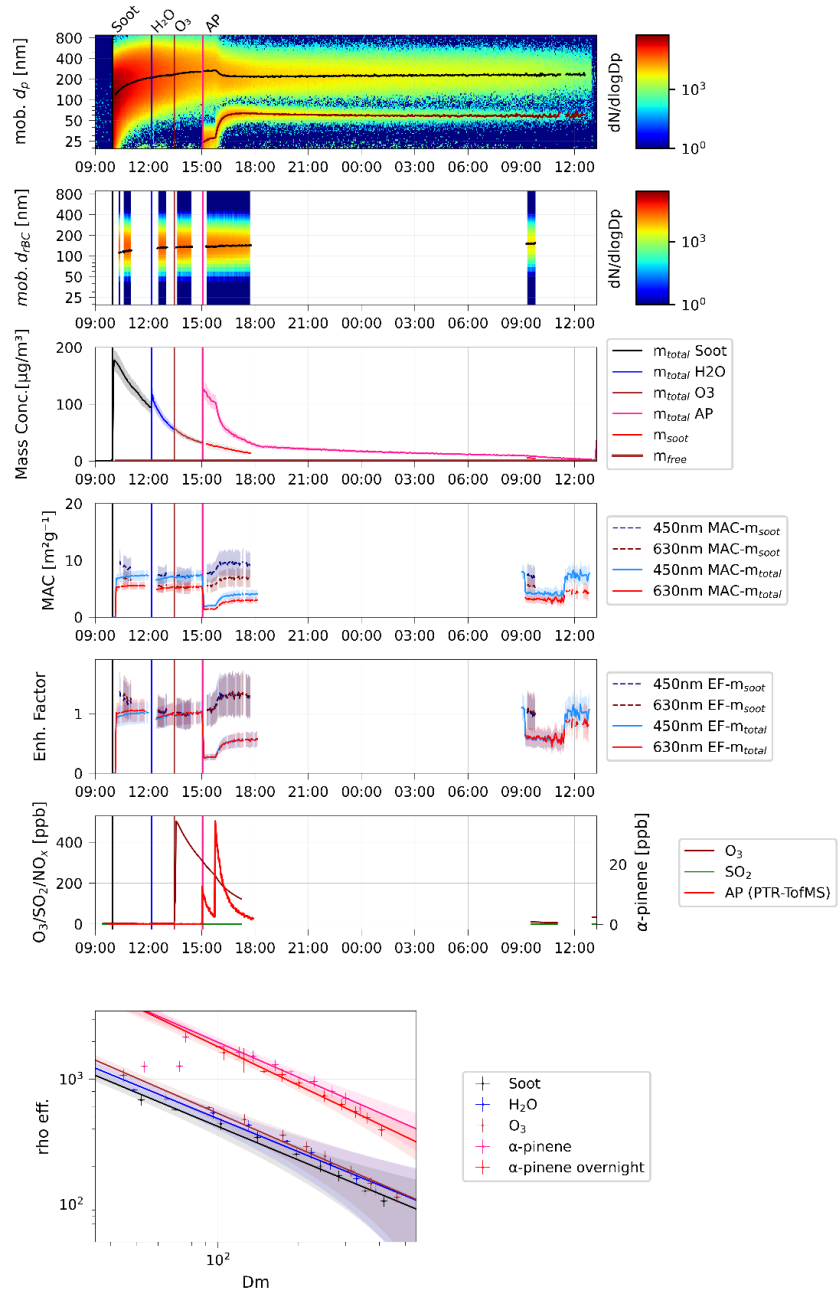
289

290 **Figure S14** Same as Fig. S11 for the SOA- S_{Ref} experiment.
 291



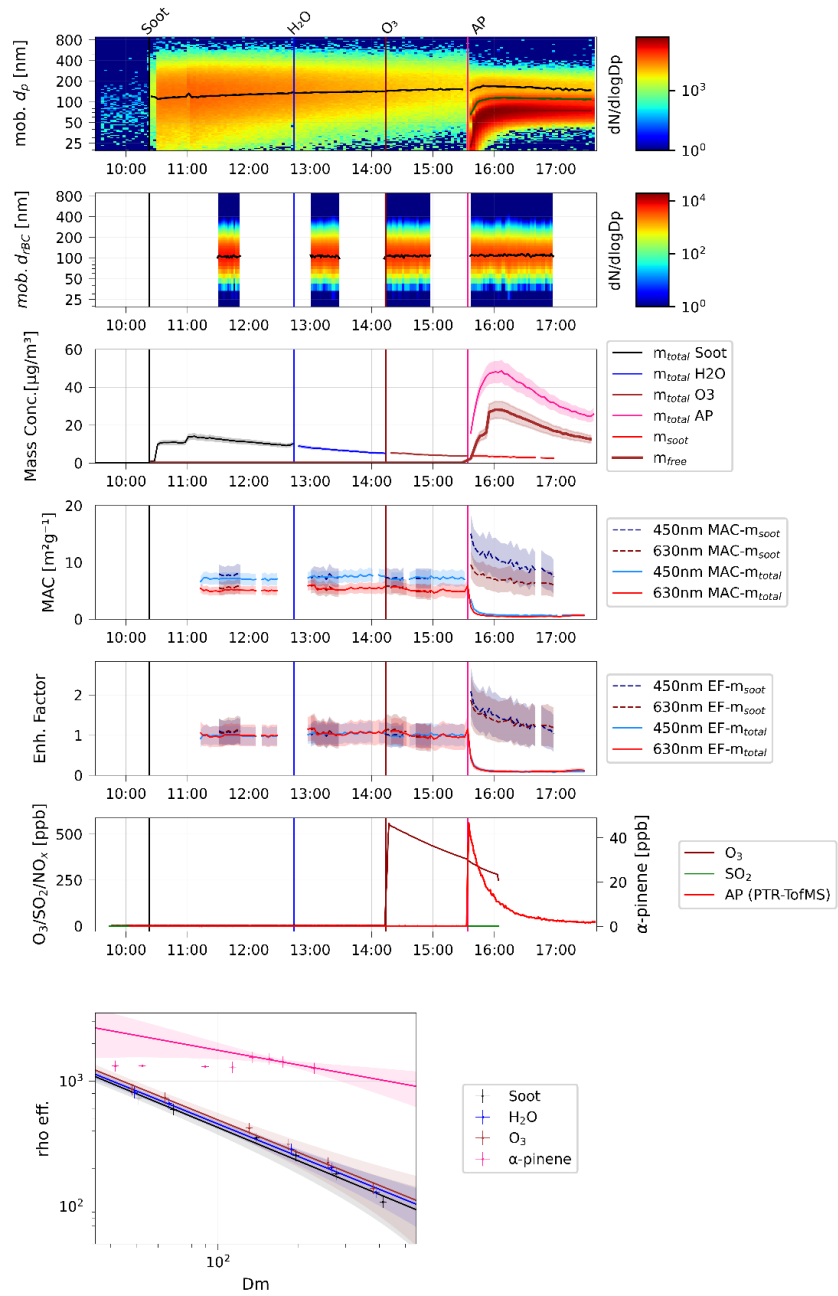
292

293 **Figure S15** Same as Fig. S11 for the SOA_{high}-S_{high} experiment.
 294



295

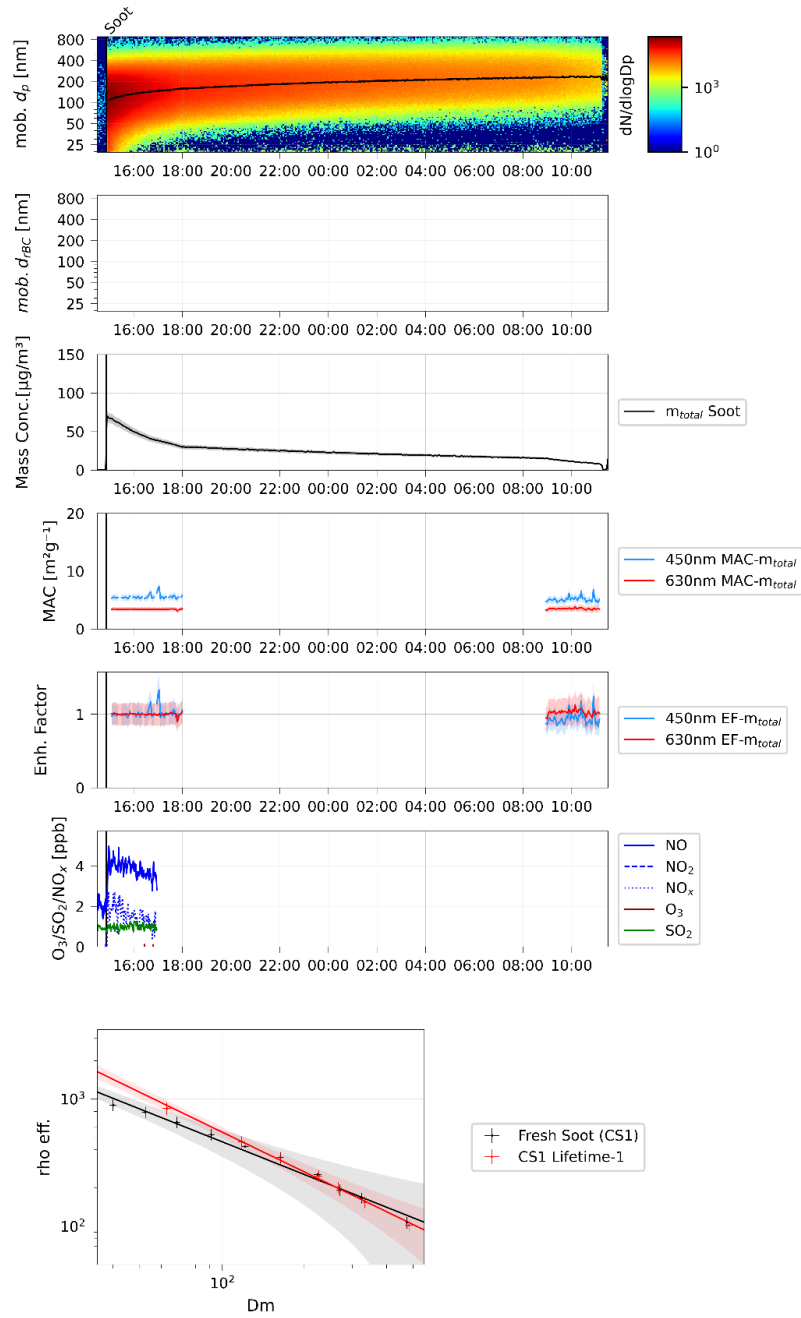
296 **Figure S16** Same as Fig. S11 for the SOA- S_{low} experiment.
 297



298

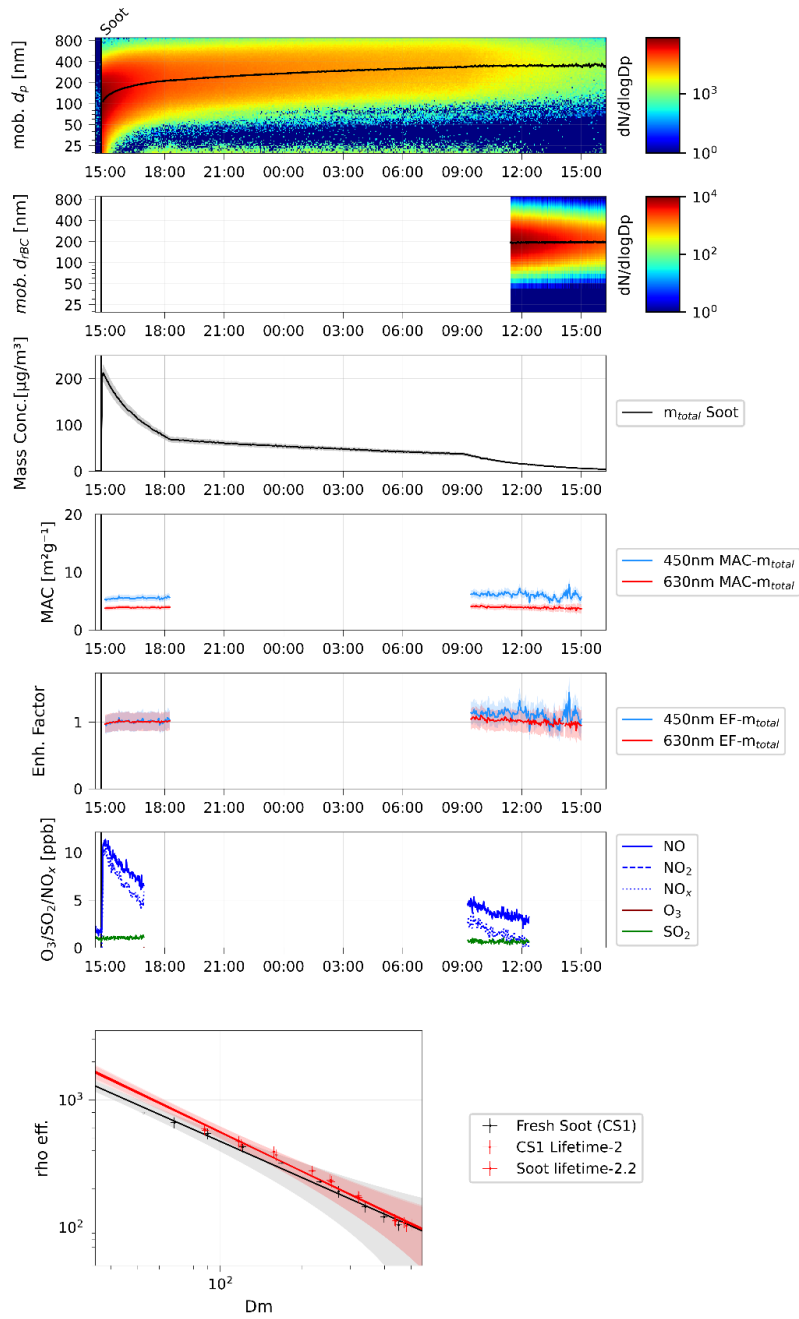
299
300

Figure S17 Same as Fig. S11 for the CS1 coagulation dry1 experiment.



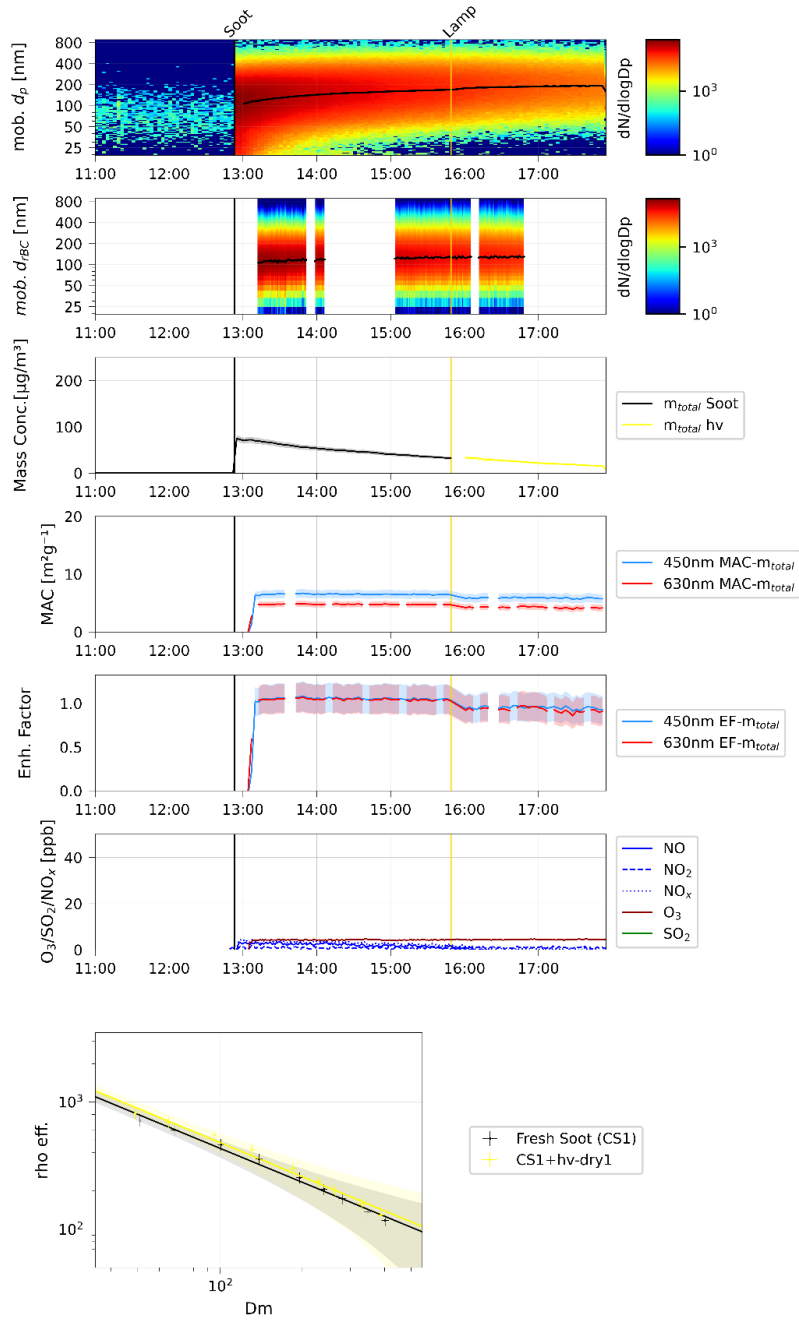
301

302 **Figure S18** Same as Fig. S11 for the CS1 coagulation dry2 experiment.
 303



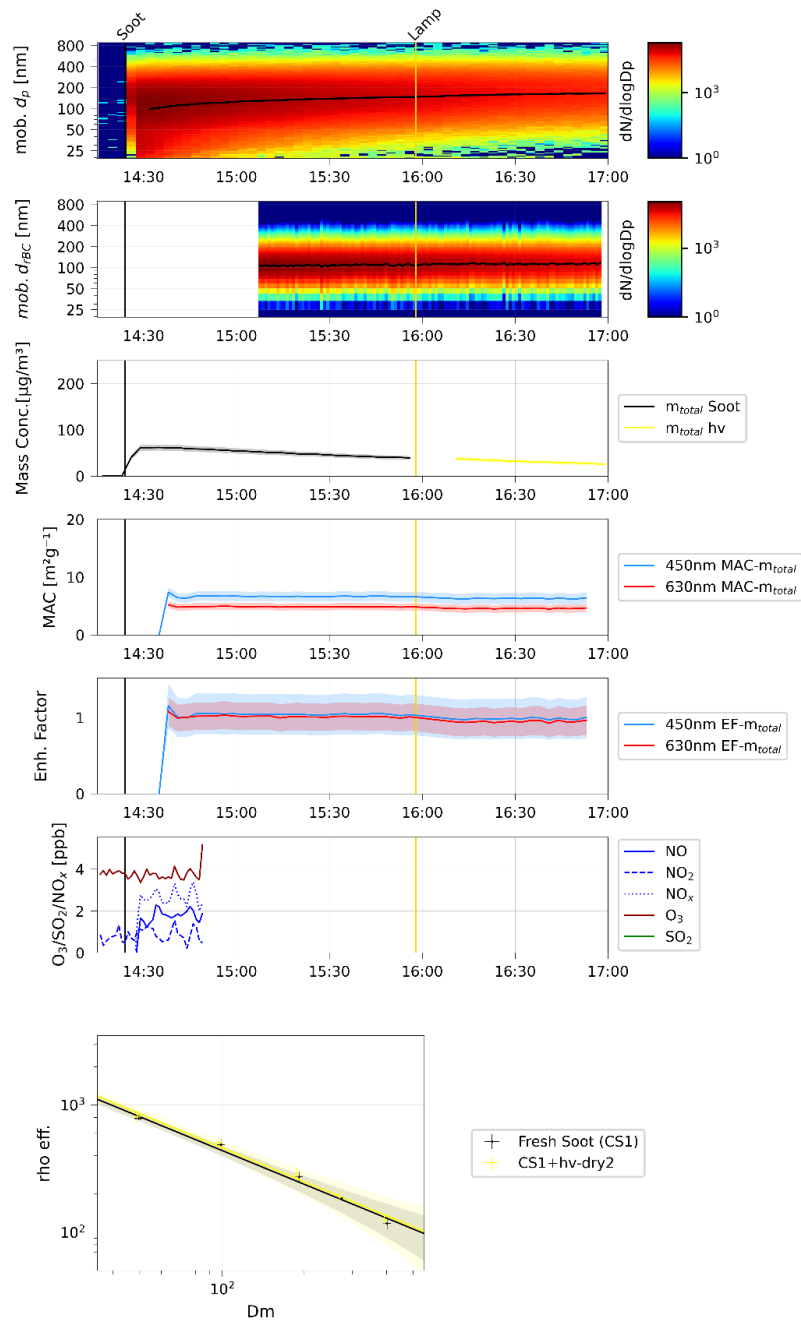
304

305 **Figure S19** Same as Fig. S11 for the CS1 irradiation dry 1 experiment.
 306



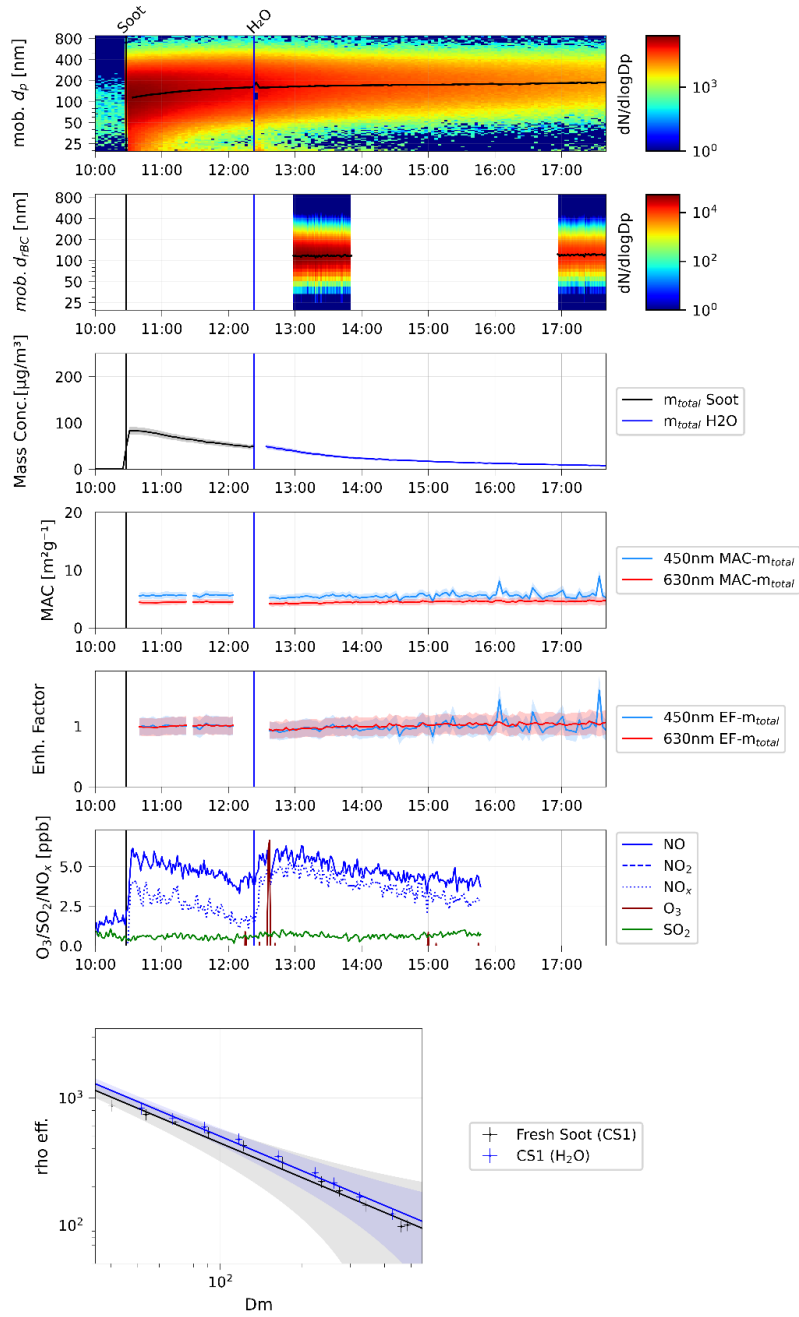
307

308 **Figure S20** Same as Fig. S11 for the CS1 irradiation dry 2 experiment.
 309



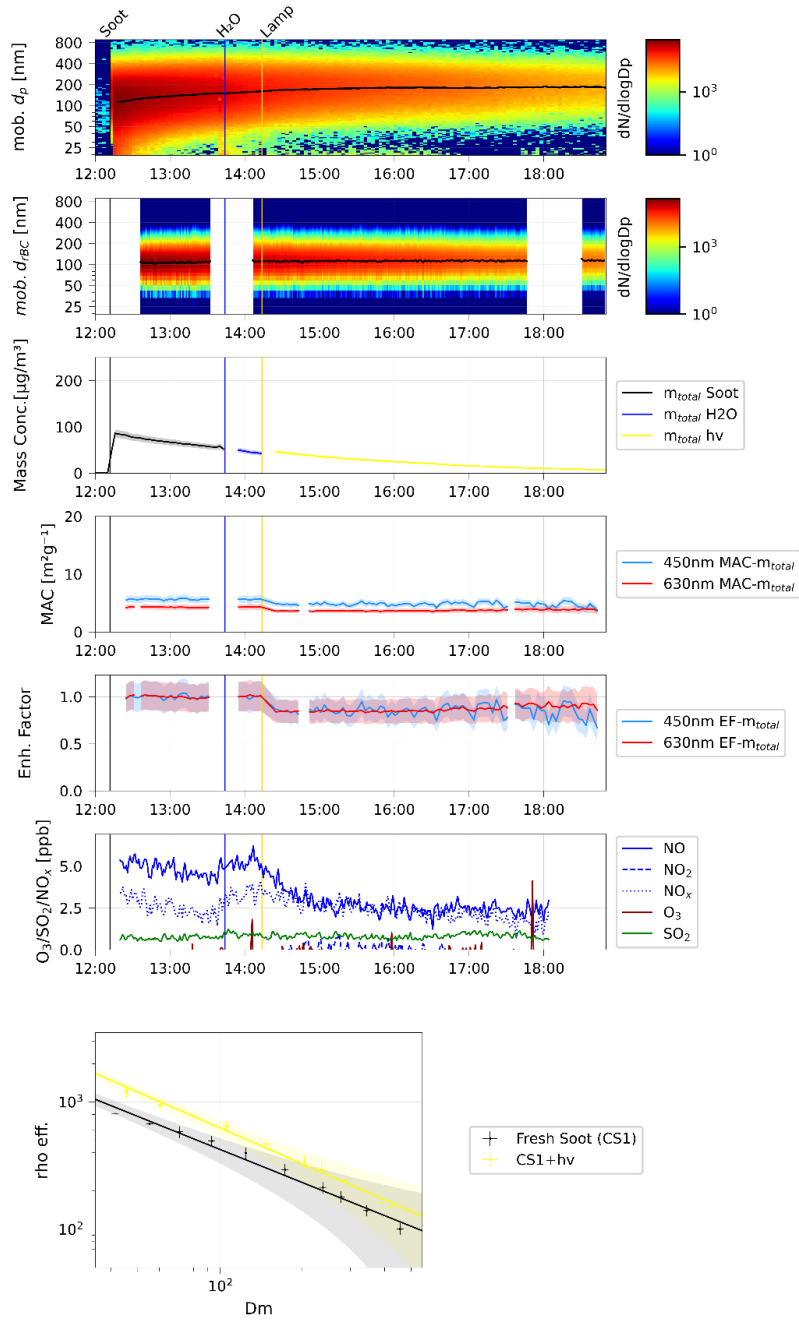
310

311 **Figure S21** Same as Fig. S11 for the CS1 coagulation humid experiment.
 312



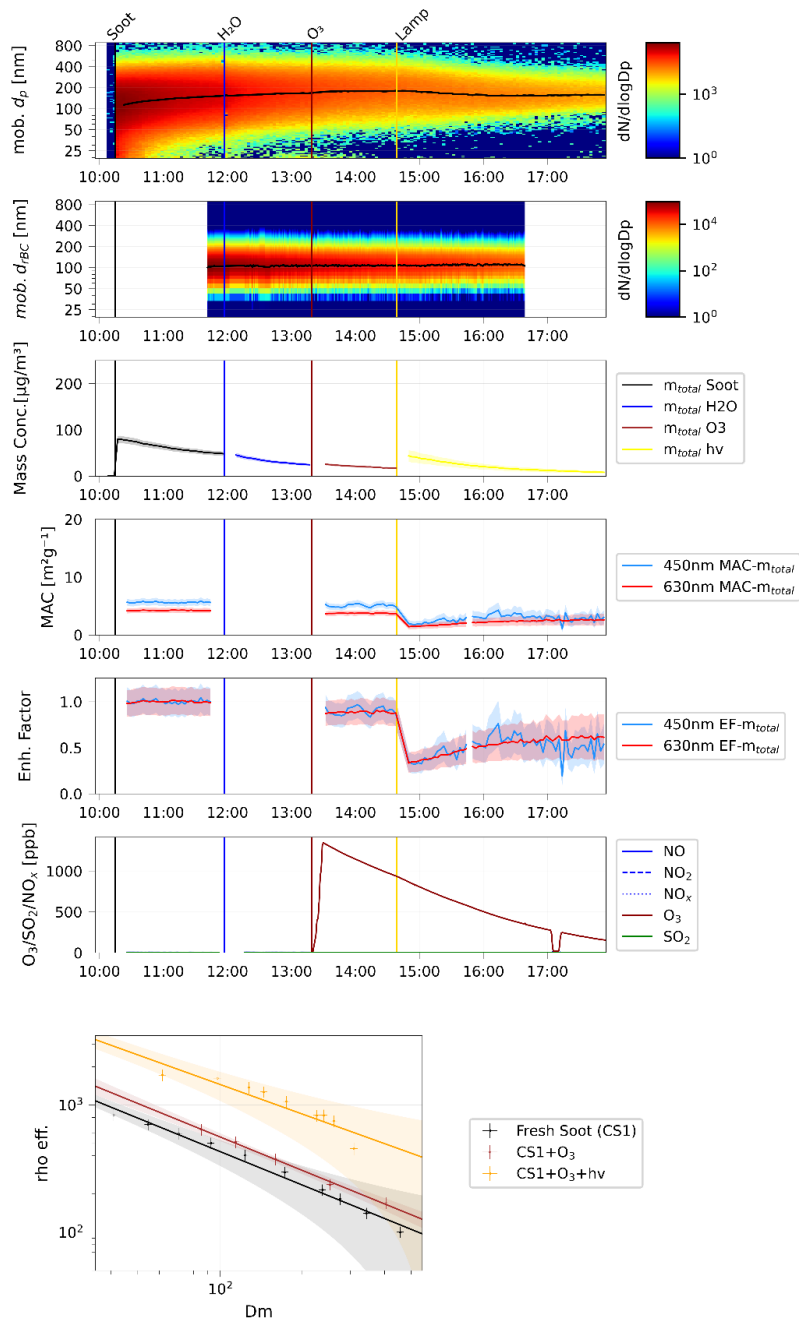
313

314 **Figure S22** Same as Fig. S11 for the CS1 irradiation humid experiment.
 315



316

317 **Figure S23** Same as Fig. S11 for the CS1 O₃ irradiation humid experiment.
 318



319

320 **Supplementary References**

- 321 Anderson, T. L., Covert, D. S., Marshall, S. F., Laucks, M. L., Charlson, R. J., Waggoner, A. P., Ogren, J.
322 A., Caldow, R., Holm, R. L., Quant, F. R., Sem, G. J., Wiedensohler, A., Ahlquist, N. A., and Bates, T. S.:
323 Performance Characteristics of a High-Sensitivity, Three-Wavelength, Total Scatter/Backscatter
324 Nephelometer, *J. Atmos. Oceanic Technol.*, 13, 967–986, [https://doi.org/10.1175/1520-0426\(1996\)013%3C0967:PCOAH%3E2.0.CO;2](https://doi.org/10.1175/1520-0426(1996)013%3C0967:PCOAH%3E2.0.CO;2), 1996.
- 326 Bescond, A., Yon, J., Ouf, F. X., Ferry, D., Delhaye, D., Gaffié, D., Coppalle, A., and Rozé, C.: Automated
327 Determination of Aggregate Primary Particle Size Distribution by TEM Image Analysis: Application to Soot,
328 *Aerosol Science and Technology*, 48, 831–841, <https://doi.org/10.1080/02786826.2014.932896>, 2014.
- 329 Bond, T. C. and Bergstrom, R. W.: Light Absorption by Carbonaceous Particles: An Investigative Review,
330 *Aerosol Science and Technology*, 40, 27–67, <https://doi.org/10.1080/02786820500421521>, 2006.
- 331 Dahneke, B.: Simple Kinetic Theory of Brownian Diffusion in Vapors and Aerosols, in: *Theory of Dispersed*
332 *Multiphase Flow*, Elsevier, 97–133, <https://doi.org/10.1016/B978-0-12-493120-6.50011-8>, 1983.
- 333 DeCarlo, P. F., Slowik, J. G., Worsnop, D. R., Davidovits, P., and Jimenez, J. L.: Particle Morphology and
334 Density Characterization by Combined Mobility and Aerodynamic Diameter Measurements. Part 1: Theory,
335 *Aerosol Science and Technology*, 38, 1185–1205, <https://doi.org/10.1080/027868290903907>, 2004.
- 336 Denjean, C., Formenti, P., Picquet-Varrault, B., Pangui, E., Zapf, P., Katrib, Y., Giorio, C., Tapparo, A.,
337 Monod, A., Temime-Roussel, B., Decorse, P., Mangeney, C., and Doussin, J. F.: Relating hygroscopicity
338 and optical properties to chemical composition and structure of secondary organic aerosol particles generated
339 from the ozonolysis of α -pinene, *Atmos. Chem. Phys.*, 15, 3339–3358, [https://doi.org/10.5194/acp-15-3339-](https://doi.org/10.5194/acp-15-3339-2015)
340 2015, 2015.
- 341 Fuchs, N. A., Daisley, R. E., Fuchs, M., Davies, C. N., and Straumanis, M. E.: *The Mechanics of Aerosols*,
342 *Physics Today*, 18, 73–73, <https://doi.org/10.1063/1.3047354>, 1965.
- 343 Habib, Z. G. and Vervisch, P.: On The Refractive Index of Soot at Flame Temperature, *Combustion Science*
344 *and Technology*, 59, 261–274, <https://doi.org/10.1080/00102208808947100>, 1988.
- 345 Heuser, J., Di Biagio, C., Yon, J., Cazaunau, M., Bergé, A., Pangui, E., Zanatta, M., Renzi, L., Marinoni, A.,
346 Inomata, S., Yu, C., Bernardoni, V., Chevaillier, S., Ferry, D., Laj, P., Maillé, M., Massabò, D., Mazzei, F.,
347 Noyalet, G., Tanimoto, H., Temime-Roussel, B., Vecchi, R., Vernocchi, V., Formenti, P., Picquet-Varrault,
348 B., and Doussin, J.-F.: Spectral optical properties of soot: laboratory investigation of propane flame particles
349 and their link to composition, *Atmos. Chem. Phys.*, 25, 6407–6428, [https://doi.org/10.5194/acp-25-6407-](https://doi.org/10.5194/acp-25-6407-2025)
350 2025, 2025.
- 351 Keabian, P. L., Robinson, W. A., and Freedman, A.: Optical extinction monitor using cw cavity enhanced
352 detection, *Review of Scientific Instruments*, 78, 063102, <https://doi.org/10.1063/1.2744223>, 2007.
- 353 Kim, H., Barkey, B., and Paulson, S. E.: Real refractive indices of α - and β -pinene and toluene secondary
354 organic aerosols generated from ozonolysis and photo-oxidation: REFRACTIVE INDICES OF ORGANIC
355 AEROSOLS, *J. Geophys. Res.*, 115, <https://doi.org/10.1029/2010JD014549>, 2010.
- 356 Laborde, M., Schnaiter, M., Linke, C., Saathoff, H., Naumann, K.-H., Möhler, O., Berlenz, S., Wagner, U.,
357 Taylor, J. W., Liu, D., Flynn, M., Allan, J. D., Coe, H., Heimerl, K., Dahlkötter, F., Weinzierl, B., Wollny,
358 A. G., Zanatta, M., Cozic, J., Laj, P., Hitzenberger, R., Schwarz, J. P., and Gysel, M.: Single Particle Soot
359 Photometer intercomparison at the AIDA chamber, *Atmos. Meas. Tech.*, 5, 3077–3097,
360 <https://doi.org/10.5194/amt-5-3077-2012>, 2012.
- 361 Massabò, D., Bernardoni, V., Bove, M. C., Brunengo, A., Cuccia, E., Piazzalunga, A., Prati, P., Valli, G.,
362 and Vecchi, R.: A multi-wavelength optical set-up for the characterization of carbonaceous particulate matter,
363 *Journal of Aerosol Science*, 60, 34–46, <https://doi.org/10.1016/j.jaerosci.2013.02.006>, 2013.

364 Massoli, P., Murphy, D. M., Lack, D. A., Baynard, T., Brock, C. A., and Lovejoy, E. R.: Uncertainty in Light
365 Scattering Measurements by TSI Nephelometer: Results from Laboratory Studies and Implications for
366 Ambient Measurements, *Aerosol Science and Technology*, 43, 1064–1074,
367 <https://doi.org/10.1080/02786820903156542>, 2009.

368 Massoli, P., Kebejian, P. L., Onasch, T. B., Hills, F. B., and Freedman, A.: Aerosol Light Extinction
369 Measurements by Cavity Attenuated Phase Shift (CAPS) Spectroscopy: Laboratory Validation and Field
370 Deployment of a Compact Aerosol Particle Extinction Monitor, *Aerosol Science and Technology*, 44, 428–
371 435, <https://doi.org/10.1080/02786821003716599>, 2010.

372 Olfert, J. S. and Collings, N.: New method for particle mass classification—the Couette centrifugal particle
373 mass analyzer, *Journal of Aerosol Science*, 36, 1338–1352, <https://doi.org/10.1016/j.jaerosci.2005.03.006>,
374 2005.

375 Onasch, T. B., Massoli, P., Kebejian, P. L., Hills, F. B., Bacon, F. W., and Freedman, A.: Single Scattering
376 Albedo Monitor for Airborne Particulates, *Aerosol Science and Technology*, 49, 267–279,
377 <https://doi.org/10.1080/02786826.2015.1022248>, 2015.

378 Otto, E. and Fissan, H.: Brownian coagulation of submicron particles, *Advanced Powder Technology*, 10, 1–
379 20, [https://doi.org/10.1016/S0921-8831\(08\)60453-7](https://doi.org/10.1016/S0921-8831(08)60453-7), 1999.

380 Otto, E., Fissan, H., Park, S. H., and Lee, K. W.: The log-normal size distribution theory of brownian aerosol
381 coagulation for the entire particle size range, *Journal of Aerosol Science*, 30, 17–34,
382 [https://doi.org/10.1016/S0021-8502\(98\)00038-X](https://doi.org/10.1016/S0021-8502(98)00038-X), 1999.

383 Park, S. H., Lee, K. W., Otto, E., and Fissan, H.: The log-normal size distribution theory of brownian aerosol
384 coagulation for the entire particle size range, *Journal of Aerosol Science*, 30, 3–16,
385 [https://doi.org/10.1016/S0021-8502\(98\)00037-8](https://doi.org/10.1016/S0021-8502(98)00037-8), 1999.

386 Petzold, A. and Schönlinner, M.: Multi-angle absorption photometry—a new method for the measurement
387 of aerosol light absorption and atmospheric black carbon, *Journal of Aerosol Science*, 35, 421–441,
388 <https://doi.org/10.1016/j.jaerosci.2003.09.005>, 2004.

389 Petzold, A., Schloesser, H., Sheridan, P. J., Arnott, W. P., Ogren, J. A., and Virkkula, A.: Evaluation of
390 Multiangle Absorption Photometry for Measuring Aerosol Light Absorption, *Aerosol Science and
391 Technology*, 39, 40–51, <https://doi.org/10.1080/027868290901945>, 2005.

392 Schnaiter, M., Linke, C., Möhler, O., Naumann, K. -H., Saathoff, H., Wagner, R., Schurath, U., and Wehner,
393 B.: Absorption amplification of black carbon internally mixed with secondary organic aerosol, *J. Geophys.
394 Res.*, 110, 2005JD006046, <https://doi.org/10.1029/2005JD006046>, 2005.

395 Seinfeld, J. H. and Pandis, S. N.: *Atmospheric chemistry and physics: from air pollution to climate change*,
396 Third edition., John Wiley & Sons, Hoboken, New Jersey, 1 pp., 2016.

397 Stephens, M., Turner, N., and Sandberg, J.: Particle identification by laser-induced incandescence in a solid-
398 state laser cavity, *Appl. Opt.*, 42, 3726, <https://doi.org/10.1364/AO.42.003726>, 2003.

399 Vecchi, R., Bernardoni, V., Paganelli, C., and Valli, G.: A filter-based light-absorption measurement with
400 polar photometer: Effects of sampling artefacts from organic carbon, *Journal of Aerosol Science*, 70, 15–25,
401 <https://doi.org/10.1016/j.jaerosci.2013.12.012>, 2014.

402 Yon, J., Bescond, A., and Ouf, F.-X.: A simple semi-empirical model for effective density measurements of
403 fractal aggregates, *Journal of Aerosol Science*, 87, 28–37, <https://doi.org/10.1016/j.jaerosci.2015.05.003>,
404 2015.